Axial cyclic and static behavior of FRP composite seawater sea-sand concrete piles ended in rock socket

by

Numan Malik (Ph.D. Candidate)
Department of Civil and Environmental Engineering, The Hong Kong Polytechnic University,
Hong Kong, China. Email: numan.malik@connect.polyu.hk

Wen-Bo Chen (Ph.D., Professor, Corresponding Author)
The College of Civil and Transportation Engineering, Shenzhen University, China
Email: geocwb@gmail.com; wenbochen@szu.edu.cn

Ze-Jian Chen (Ph.D., Research Assistant Professor)
Department of Civil and Environmental Engineering, The Hong Kong Polytechnic University,
Hong Kong, China
Email: zejchen@polyu.edu.hk

Pei-Chen Wu (Ph.D., Research Assistant Professor)
Department of Civil and Environmental Engineering, The Hong Kong Polytechnic University,
Hong Kong, China. Email: elvis.wu@polyu.edu.hk

and
Jian-Hua Yin (Ph.D., Chair Professor)
Department of Civil and Environmental Engineering
Research Institute for Land and Space
The Hong Kong Polytechnic University, Hong Kong, China. Email: cejhyin@polyu.edu.hk

Revised manuscript submitted to *Journal of Geotechnical and Geoenvironmental Engineering*
for possible publication as an original research paper

Abstract

Pile foundations supporting high-rise buildings are generally subject to cyclic loading because of dynamic loading. The corrosion of steel materials in pile foundations is another major concern, especially for piles in a marine environment. In this study, a series of cyclic and static loading tests on the model piles made of fiber-reinforced polymer (FRP) and sea sand-seawater concrete (SSC) and ended in a rock socket were reported. Three structural configurations (FRP tube confined, FRP rebar cage reinforced, and centered FRP rebar reinforced) were adopted for model piles. The strain along the depth of model piles was measured using fiber Bragg grating (FBG) optic sensors and an advanced distributed optical sensing technique, optical frequency domain reflectometry (OFDR). The strain distribution, axial cyclic stiffness, and shaft friction mobilization of piles under static and different modes of axial cyclic loading were analyzed and explored in detail. The test results indicate that the FRP tube confined model pile showed higher confinement and cyclic capacity and lower stiffness degradation, leading to relatively more stable behavior. A high level of cyclic loading can cause micro-cracks to form and grow within the pile material, thereby decreasing the pile stiffness. The strain profile of all the piles along the depth appeared to follow a similar trend and fluctuations at certain points that led to the failure of piles. The cyclic stiffness showed gains initially when cyclic load conditions were below a certain threshold level but degraded when loading was increased beyond it. Besides, the shaft resistance gradually increased with cycles with higher mobilization in the upper portion of the socket. The data from experiments have provided the first systematic study on the performance of the FRP-SSC composite model piles ended in rock sockets under static and axial cyclic loadings and for the development of a potential predictive method for pile settlement and capacity for the better design of rock-socketed piles.

KEYWORDS: Rock-socketed piles; FRP composites; sea-sand seawater concrete; optical fiber sensing; cyclic and static loading.

1 Introduction

Bored concrete piles with pile ends socketed in bedrock (rock-socketed piles) are commonly adopted for bridges, multi-story buildings, elevated highways, and offshore platforms with stringent requirements for bearing capacity and settlement control. In Hong Kong (HK), rock-socketed piles are a prevalent foundation type for medium- or high-rise buildings like the Cullinan (270 m) and Nina Tower (319 m) (Sze, 2015) due to the shallow depth of bedrock in waterfront areas. The bearing capacity of a rock-socketed pile consists of shaft and base resistance, which normally will not be mobilized simultaneously (Ng et al., 2001). The load transfer behavior of a rock-socketed pile depends on the properties of the pile shaft, rock mass stiffness, and the behavior of the pile-rock interface, considering elastic solutions. The pile-rock interface usually behaves differently from the pile or rock material, showing a non-linear response. The load transfer behavior of a rock-socketed pile is dependent on the properties of pile shaft, rock mass stiffness, and the behavior of the pile-rock interface considering elastic analysis. Pells and Turner (1979) provided a design chart of the ratio between bearing capacity and shaft resistance considering the varying aspect ratio of the socket (socket depth/pile diameter of 0.25~4) and stiffness ratio between pile and rock (0.25~1000). Generally, shaft resistance is fully mobilized at a displacement of 0.5-1.5% of pile diameter, while 10-20% is required for base resistance (Haberfield and Collingwood, 2006). Carter and Kulhawy (1988) reported that shaft resistance normally accounts for 80-90% of capacity, provided the pile is under service loading with relatively small displacement. Extensive efforts (Williams and Pells, 1981; Horvath et al., 1983; Rowe and Armitage, 1987; McVay et al., 1992; Kulhawy and Phoon, 1993; O'Neill and Hassan, 1993; Song and Pei, 2022) have been spent in correlating shaft resistance with the unconfined compressive strength (UCS) of rock or concrete, whichever is lower. Besides, several factors control the development of shaft resistance, including shaft diameter, side surface roughness, rock stiffness, and construction practices (e.g., drilling fluid residue and smear), enabling designers to take a conservative approach to estimate shaft resistance. In HK, the Geotechnical Engineering Office (GEO) (1996) suggested that the empirical relationship proposed by Horvath et al. (1983) be used to calculate shaft resistance using a minimum mobilization factor of 1.5 in consideration of possible incompetent pile base conditions. According to the Code of Practice for Foundations (Building Department, 2017), the presumed allowable friction between rock and concrete for piles is capped at 700 kPa, significantly smaller than the estimated value from the above-mentioned empirical correlations. An in-depth study of field tests on grouted piles in sandstone by Klapper et al. (2020) and Manceau et al. (2021) revealed that shaft resistance is inversely proportional to rock socket diameter, which was not acknowledged in the previous classical models. For onshore or offshore large-diameter grouted, bored, or drilled piles, this ignorance of the inverse relationship with diameter will likely result in an overestimation of shaft resistance. In addition, empirical relationships usually can only be applied to the cases based on which they were proposed, indicating the site-specific essence of those correlations. Given the spatial variability of ground and high cost in field tests, it is challenging to investigate the behavior of shaft resistance under complex applied loadings qualitatively and quantitatively. In this study, physical model tests were adopted because of their advantages in better-controlled boundary conditions, including loading and deformation, and convenience for parametric studies.

Pile foundations are often subjected to cyclic loadings caused by wind, water currents, waves, earthquakes, traffic loads, and ice sheets. Cyclic loadings are variable and repeated in nature with a different range of magnitudes and cycles. For instance, offshore wind turbines generate millions of rotating blade cycles on supporting piles (Jardine et al., 2013), and pile foundations supporting the transport system always experience significant axial cyclic loads (Copsey et al., 1989). Chan and Hanna (1980) found that the cyclic behavior of piles in the sand is influenced by major cyclic loading parameters such as frequency, cyclic amplitude, mean load values, the number of cycles, and loading history. The cyclic stiffness, stability diagrams, and settlement features of piles in the sand under a variety of axial cyclic loading modes (stable, unstable, and metastable modes) were studied. Previous researchers adopted the classical cyclic interaction loading diagram to characterize the cyclic loading tests based on cyclic stability criteria. This practice has been applied widely in the piles driven in sand and clays (Jardine and Standing, 2012; Tsuha et al., 2012; Rimoy et al., 2013; Buckley et al., 2018) and field tests of drilled and grouted piles in rock (Klapper et al., 2020; Manceau et al., 2021). Helical pulldown micro piles reinforced by fiber-reinforced polymer (FRP)-steel fiber show the degradation of shaft resistance under cyclic loads (El Sharnouby and El Naggar, 2012).

On the other hand, Le Kouby et al. (2004) and Jardine et al. (2006) claimed that optimizing cyclic loading amplitude improved the bearing capacity of piles. Bekki et al. (2013) also stated that the shaft friction of piles exhibited strain hardening owing to shear dilatancy under a large number of loading cycles. Zhang et al. (2016) asserted that the cyclic stiffness of soft rock-socketed piles first increases then decreases, and finally tends to level off as the cycle number increases with the progressive damaging process of soft rock interface. Although numerous research works have been carried out on the cyclic response of piles in sand, silt, and soft soils, the behavior of piles ended in rock-socket under cyclic loading, with emphasis on the cyclic stiffness variation of pile body and pile-rock interface, is rarely reported. It is necessary to deeply study cyclic loading tests on rock-socketed piles based on systematic tests to provide guidance and potential predictive measures.

Reinforced concrete materials used for piling in harsh marine environments are susceptible to significant steel corrosion and concrete deterioration. The corrosion of steel reinforcement further induces cracks in concrete, reducing its effective area and its bonding with concrete, resulting in various issues such as spalling, structural failure, and substantial maintenance expenses. For example, Krauss and Nmai (1996) pointed out that most bridges that are along coastlines or offshore and rely on pile foundations will experience premature concrete degradation and steel corrosion in the first 12 years of their service life. Over the last several decades, FRP, a substitute for steel materials, has gained increasing popularity thanks to its high strength-to-weight ratio (one-fifth that of steel) and immunity to corrosion. Over 300 bridges founded on pile foundations were constructed using FRP reinforcement in Canada and the United States in the last three decades (Nolan et al., 2021). Besides that, the tremendous volume of river sand exploitation in the conventional concrete industry poses a serious threat to the environment (Xiao et al., 2017). Given this, desalted sea sand has been used in concrete structures worldwide, including in Japan, China, and the United Kingdom. However, the extra cost and consumption of freshwater in the desalting process hinder the wide application of sea sand. FRP does not exhibit significant long-term degradation in typical marine environments (Li et al., 2018), making it a promising alternative to steel as a reinforcing material in sea sand-seawater concrete (SSC). Considerable efforts have been put into the structural behavior of concrete-filled FRP composite piles, particularly concrete-filled FRP tube piles (Mirmiran et al., 1999; Fam et al., 2003; Sakr et al., 2004; Juran & Komornik, 2006; Pando et al., 2006; Park et al., 2011). Filling concrete can support overcoming the local buckling of FRP tubes, providing lateral confinement to increase the strength and ductility of concrete. Zyka and Mohajerani (2016) concluded that concrete-filled FRP tube piles possess excellent load-bearing capacity, relatively low prices compared with other composite piles, and a wide range of available sizes. Additionally, FRP tubes can be designed with different laminated structures to resist various external load combinations, rendering extra steel reinforcement unnecessary and reducing life-cycle costs. The lightweight FRP tubes can largely ease construction.

In this paper, the cyclic performance of the proposed innovative and sustainable design of FRP-confined SSC piles installed in a rock socket was investigated through a series of physical model tests. Physical model piles with different typical configurations were cast in a rock socket and subjected to cyclic loadings of different cyclic amplitudes and mean loads to determine the characteristics of cyclic stiffness and shaft friction mobilization. The effects of cyclic loading history on the compression behavior of piles under subsequent monotonic and cyclic loadings will also be investigated. Fiber Bragg grating (FBG) optic sensors provided discrete static or cyclic strain information along the length of piles inside and above the rock socket. Moreover, a novel fully distributed sensing technology named optical frequency domain reflectometry (OFDR) with a higher spatial resolution of 1 mm and a high sensing accuracy of ±1 με was used to capture the continuous strain profile of piles inside the rock socket. The data from experiments have provided the first systematic study on the performance of the FRP-SSC composite model piles installed in rock socket under static and axial cyclic loadings. The findings from this study are significant for formulating a potential predictive method for estimating pile settlement and capacity, leading to better designs for rock-socketed piles in the future. Therefore, the results can be generalized considering the scale effects, test conditions, and parameters for the actual field conditions.

2 Experimental Program

2.1 Setup and design of physical model piles

An innovative physical model was designed and built at the Soil Mechanics Laboratory of The Hong Kong Polytechnic University (PolyU), as shown in Fig. 1. This system is composed of a hydraulic loading actuator (GCTS, the United States of America) that can apply both static and cyclic loads axially on the pile head. A steel reaction frame was designed to support the hydraulic loading actuator. Model piles were constructed in a steel tank, which has an inner diameter of 1 m and an inner depth of 1.326 m. A hardened gypsum layer was laid at the bottom of the steel tank to position and hold the granite rock at the center. A socket with a diameter of 100 mm and a depth of 160 mm was drilled into the rock with an inbuilt roughness of 5 mm based on the Monash Roughness Model (Seidel and Collingwood, 2001). Rock sockets for five model piles were manufactured in a workshop such that the inbuilt roughness was identical for all tests. The granite rock base was designed with a larger contact area for the uniform distribution of loads in a similar way as in the field. The length-to-diameter ratio of the socket was kept at 1.5, lying within the range of common engineering practices (Ng et al., 2001). As the rock socket was prepared with an intact rock mass with very high strength and stiffness, the pile-influencing region in the rock is believed to be small.

Five model piles were tested for which geometric similarity was considered in the design. Table 1 presents the similarity relations for the model and prototype with a scaling ratio, n, which is defined by the ratio of the diameter range of full-scale piles in the field to that in the physical model. Therefore, in this study, n varies from 6 to 25, as the common range of rock socketed pile diameter is 0.6 to 2.5 m in Hong Kong (Zhan and Yin, 2000; Chen et al., 2021b). The effects of density, gravity, and rate dependency on the scaled model were not investigated in this study. Two linear variable differential transformers (LVDTs) were fixed to an independent reference frame near the pile head to monitor the overall pile head displacement of model piles under axial loading, as shown in Fig. 1. Note that there is no soil surrounding the model piles for all five model tests.

Model piles with different configurations were investigated in this study. They all have a length of 1460 mm, of which 160 mm was embedded in the rock socket and 1,300 mm was above the rock surface. Piles 1 and 2 comprise an SSC column confined by a glass fiber reinforced polymer (GFRP) tube possessing a thickness of 3.5 mm, an internal diameter of 100 mm, and a total length of 1300 mm, as shown in Fig. 2. Note that a specially designed clamp collar was fixed at tube bottom to increase the base stability of tube and steel wires attached to the tank were used to fix tube horizontally such that the GFRP tube was kept firmly and annual inner wall of tube can be aligned with rock socket almost perfectly. In addition, the GFRP tube was sealed with water-resistant adhesives that would be removed after SSC curing near the rock surface to prevent any gap between the tube and the rock surface. Fig. 3 shows that Pile 3 was made of SSC that is 100 mm in diameter with four longitudinal GFRP rebars embedded (a diameter of 9.5 mm and a length of 1460 mm). Above the rock socket, rebars were confined by circular stirrups of an outer diameter of 90 mm with a center-to-center spacing of 70 mm. In model Pile 4, a longitudinal GFRP rebar with a diameter of 19 mm was positioned at the center and surrounded by the SSC column with a diameter of 100 mm, as shown in Fig. 4. Pile 5 was designed in the same way as Pile 4, except that a 10 mm debris (loose completely decomposed granite with diameter smaller than 10 mm) was placed at the socket bottom of the former to simulate debris in common construction site. For the third model pile, the rebar cage was first fabricated and then fixed in the rock socket within the polyvinyl chloride formwork casing, followed by the casting of the SSC inside. In the design of model piles, the GFRP tube was considered as confinement to the SSC in both axial and hoop directions and worked as a permanent casing. The longitudinal rebars, along with concrete, contributed to the capacity of the pile against axial loads. Circular ties provided confinement to avoid the buckling and shear failure of longitudinal rebars. The SSC was filled using a small trowel into the rock socket and the GFRP tube from the upper side. The filled SSC was vibrated manually with an aluminum rod (1 cm diameter) during the casting process without any changes in the optical sensors position.

2.2 Materials

A specially designed mix ratio of SSC was used for constructing model piles, as shown in Table 2. To increase workability and sustainability, superplasticizers and fly ash were employed in the mix design. Sea sand and seawater were collected from the Chek Lap Kok area of Hong Kong. Previous research studies indicated that sea sand contains high contents of silt or clay particles, which affect the workability and strength of concrete. Therefore, the sea sand was washed first to remove the clay particles, and afterward, it was kept in an oven at 105℃ for 48 hours. The dried sand was then sieved through a 5 mm sieve to remove the unwanted large aggregates. The particle size distribution curve of washed sea sand is given in Fig. 5 below. Besides, the natural seawater has PH and salinity of 7.92 and 32.241 g/L, respectively. Table 3 shows the results of ion composition from ion chromatography (IC) tests.

To check the mechanical properties of the SSC, uniaxial compressive tests were carried out on cylindrical specimens with a height of 100 mm and a diameter of 50 mm. Strain gauges were adopted to measure the strain of each specimen. The axial stress-strain curve measured with strain gauges fitted well with the Comite Euro-International du Beton–Federation International de la Precontrainte (CEB-FIP) Model Code (Code, 1990) developed on the relations formulated by Sargin and Handa (1969):

$$\frac{\sigma_c}{f_{cm}} = \frac{A\eta - \eta^2}{1 + (A-2)\eta}, \eta = \frac{\varepsilon_c}{\varepsilon_{cm}}, A = \frac{E_c}{f_{cm} / \varepsilon_{cm}} \tag{1}$$

where σ_c represents axial stress; f_{cm} stands for the peak stress (f_{cm} = 31 MPa); ε_c refers to axial strain; ε_{cm} denotes the strain at f_{cm} (ε_{cm} = 0.00344); E_c is the initial elastic modulus (E_c = 22.9 GPa). The tangent modulus $E_t = \frac{d\sigma_c}{d\varepsilon_c}$ varied according to Eq. (1), which was adopted for calculating the axial force of piles based on the strain value measured by optical sensors in Section 3.7.

Two different types of GFRP composites, namely tube and rebar, were used for four model piles. Piles 1 and 2 have the same configuration with a 3.5 mm thick GFRP tube used for confining the SSC, as shown in Fig. 2(b). Model Pile 3 has four rebars confined with circular ties, while Piles 4 and 5 have a single-centered rebar, as shown in Figs. 3(b) and 4(b), respectively. The GFRP tubes are filament-wound tubes manufactured from E-glass fiber and vinyl ester resin with a fiber orientation of ±45°. Axial compression tests were conducted on small specimens of FRP tubes, cut from the same tube used in the model pile, having a height of 60 mm and a thickness of 3.5 mm. The axial and hoop elastic moduli obtained are 11.3 and 10.1 GPa, respectively. The rebars used in Pile 3 were made from unsaturated polyester resin and E-glass fiber coated with sand, possessing an elastic modulus of 50.8 GPa, according to the manufacturer’s report. Uniaxial compression tests were performed on six specimens (having 50 mm diameter and 100 mm height) of granite rock and hardened gypsum plaster specimens. Based on ASTM C469, the Young's modulus (*E*) and uniaxial compressive strength (UCS) of the granite rock were determined as 42 GPa and 177 MPa, respectively, while those of the gypsum plaster were 22 GPa and 60 MPa, respectively. The rock socket was manufactured commercially and classified as Grade I rock according to Geoguide 3 in Hong Kong.

2.3 Advanced optical fiber sensing technique

All the model piles were instrumented with an advanced distributed optical fiber sensing (DOFS) system to measure the strain along the pile body based on Rayleigh backscattering via the OFDR sensing technique. In the OFDR sensing system shown in Fig. 6, the continuous linearly swept output light from a tunable laser source is divided into two distinct optical paths using an optical coupler (Lin et al., 2021; Wu et al., 2022). One path serves as the reference light reflected from a mirror. The second path is utilized as the measurement light, which propagates through a sensing fiber attached to the measuring surface. As the measurement light travels in the sensing fiber, Rayleigh backscattering generates scattered light. Subsequently, this scattered light is combined with the reference light through the optical coupler, generating beat frequency interference. This interference is detected and demodulated by a photoelectric detector, enabling the measurement of strain or temperature variations along the length of the sensing fiber (Palmieri and Schenato, 2013). Strain and temperature variations are given in Eq. (2):

$$\Delta v = C_{\varepsilon}\Delta\varepsilon + C_{T}\Delta T \tag{2}$$

where $\Delta\nu$ = Rayleigh spectrum shift, $\Delta\varepsilon$ = strain change, ΔT = temperature change, and C_ε and C_T are the coefficients of strain and temperature change, respectively, which were calibrated as -0.15 GHz/με and -1.25 GHz/℃, respectively (Wu et al., 2020). However, the temperature variations were ignored due to constant temperature conditions during the tests.

In addition, multiplexed FBGs were also instrumented in model piles because of their high resolution and data acquisition frequency for cyclic loads (Chen et al. 2020a; Chen et al., 2021a; Hong et al., 2022). A multiplexed FBG system consists of multiple Fiber Bragg Gratings (FBGs) inscribed in a single optical fiber at different positions. Each FBG reflects light at a specific wavelength, enabling strain and temperature measurements at various locations along the fiber. When the incident light passed through the grating region, the variations of temperature and strain in the fiber induced a shift in the wavelength of the central light reflected from the grating region with a correlation given below:

$$\frac{\Delta\lambda}{\lambda_i} = c_1\Delta\varepsilon + c_2\Delta T \tag{3}$$

where "*i*" is the initial state, λ represents the reflected light wavelength, $\Delta\lambda$ stands for the change in wavelength, ΔT refers to temperature change, $\Delta\varepsilon$ denotes the change in strain, and c_1 and c_2 are the coefficients of strain and temperature change, respectively. In this study, the value of c_1 was regarded as 0.78, whereas temperature change was neglected because of constant temperature conditions in the laboratory. In this study, an OFDR-based interrogator (OSI-I, Junlong Technology Ltd, China) and an FBG interrogator named SM130 from MICRON OPTICS were used for sensing.

2.4 Installation and instrumentation of FBG and OFDR sensors

Model piles were instrumented with FBG sensors and OFDR fibers along the length. FBGs were employed to monitor the cyclic loading behavior of model piles due to the high frequency of data acquisition. Regarding Piles 1, 2, 4, and 5, arrays of multiplexed FBGs were attached to an aluminum channel and embedded inside the concrete, as shown in Figs. 2(b) and 4(b). The aluminum channel was designed to protect vulnerable optical fibers and form a quasi-distributed sensing strip with a finite number of FBGs. For Pile 3, the FBGs were attached to the rebar protected with glue, as shown in Fig. 3(b). For each model pile, eight FBGs were placed in the pile body above the rock socket and four FBGs within the rock socket, with a spacing of 160 and 35 mm, respectively.

For Piles 1 and 2, OFDR sensing fibers were embedded longitudinally in the SSC with six sections marked as “S1 to S6”, as shown in Fig. 3(b). As for Pile 3, two independent fibers were installed on the rebars and within the SSC, with six sections (S1 to S6 and F1-F6) for each fiber in the cross-section of the pile, as shown in Fig. 3(b). Since all the fibers worked as a sensor along the whole length, a section of the fiber (the slack fiber section) was kept free in the air to separate each measuring fiber. Slack fiber sections were mechanically strain-free, allowing locating the position of the measured strain from the strain distribution curves of the entire fiber. Measuring fibers were pre-tensioned and then glued on the GFRP tube and rebars using an ultra-high-strength epoxy adhesive to protect sensing fibers and ensure a good bond between the fiber and surface. Pre-tensioning the measuring fibers ensures a stable state prior to loading. A pre-tension within the range of 50 to 100 micro strain was applied which was measured and recorded with OFDR interrogator. A 3 mm notch was made on GFRP rebars to properly place the sensing fiber, as shown in Fig. 4(b). Table 4 lists the details of the configuration, materials, and instrumentation of five model piles.

2.5 Testing program

Model piles were cured with seawater under room temperature for 28 days and then subjected to a series of cyclic loading tests applied by a GCTS hydraulic loading system. Before loading, all the model piles were capped with high-strength gypsum to ensure that stresses were distributed evenly over the pile head. The cyclic testing programs with different cyclic amplitudes and mean loads are summarized in Table 5. In practice, piles do experience multi-round loadings with irregular loading levels. In this study, we take the influence of earlier loading tests as one of the main focuses. We investigated the loading sequence (increasing, decreasing, or repetitive) on the change of static or cyclic deformation resistance, particularly the cyclic stiffness, of pile body and rock socketed pile section, considering the effect of pile configuration. The first intention of the test design is to investigate the effect of increasing loading levels. The second intention is to see the effects of a prior larger cyclic loading level on the cyclic response of pile under subsequent lower cyclic loading level. The third intention is to reveal the effect of loading-unloading to zero on the pile deformation, which is relatively less investigated.

The Sine function cyclic loading applied to the model pile head is presented in Fig. 7. Generally, pile foundations experience cyclic loadings with frequencies ranging from 0.0001 to 0.1 Hz and 10 to 10^5 cycles (Puech, 2013). The frequency adopted in this study is 0.01 Hz with 100 cycles for each loading case. Model piles were unloaded after each stage of cyclic loading and finally subjected to axial monotonic compression under the condition of load control till failure.

3 Results and discussions

3.1 Compression of pile body under monotonic loading

The pile body compression u_{pb} was calculated by integrating the strain measured by eight FBGs along the depth of the model piles above the rock surface using the following equation:

$$u_{pb} = \int_{0}^{l_a} \varepsilon(z)dz \tag{4}$$

where l_a represents the length from the pile head to the rock surface, $\varepsilon(z)$ stands for the strain at the position with a distance of z to the pile head, and the subscript "*pb*" denotes the pile body.

The pile head load-pile body compression curves of the model piles monitored during post-cyclic monotonic loading are illustrated in Fig. 8(a). With the same structural configuration, Piles 1 and 2 presented a similar trend in the load-compression response under a load of 130 kN. When the load was increased beyond 130 kN, however, Pile 1 significantly deformed due to a technical problem, i.e., by the failure of the circular steel transferring case, resulting in the tilting of the pile. Hence, Pile 2 was discussed in detail in the following sections for the configuration of the FRP tube confined concrete pile. It can be observed that the FRP tube confined pile (Pile 2) withstood a higher load value of 240 kN compared with 215 kN of the FRP rebar cage reinforced pile (Pile 3) under the condition of the same compression value. Pile 2 exhibited more ductile behavior with the further increase of load because of the lateral confinement from the FRP tube, greatly improving the ductility and strength of concrete. Under the same loading magnitude, Pile 5 showed larger compression compared with Pile 4 due to the presence of debris in the rock socket, which reduced the pile stiffness resulting from the collapse and crushing of debris particles under higher loading levels (Chen et al., 2020b).

In Fig. 8(b), the variation of tangent modulus for Piles 2, 3, 4, and 5 with increasing pile body compression is presented. Before reaching a compression value of 0.75 mm, Piles 4 and 5 demonstrate significantly higher loading resistance compared to the other model piles. This can be attributed to the high modulus of the centered FRP rebar in these piles (50 GPa) in contrast to the modulus of concrete (22 GPa). However, starting from a compression of 0.5 mm, the tangent modulus of Piles 4 and 5 rapidly degrades, likely due to local buckling of the centered FRP rebar. In the case of Piles 2 and 3, there is an initial sharp decrease in tangent modulus, followed by a turning point at compressions of 0.14 mm for Pile 2 and 0.24 mm for Pile 3. Subsequently, both piles exhibit a period of strain hardening until reaching compression levels of approximately 1.2 mm to 1.3 mm. Throughout this range, the tangent modulus of Pile 2 remains consistently higher than that of Pile 3, indicating that the FRP tube provides greater confinement to SSC. The superior ductility of Pile 2 over Pile 3 is demonstrated by a larger compression value at which the tangent modulus starts to degrade rapidly, occurring at 1.71 mm for Pile 2 and 1.24 mm for Pile 3. Furthermore, it is noticeable that Piles 4 and 5 exhibit a slower degradation of modulus in the residual stage, followed by Pile 3 with FRP rebar stirrups and then Pile 2 with FRP tube confinement. Pile 2 almost experiences brittle failure after the rupture and buckling of the FRP tube. These findings highlight the importance of pile configuration, specifically the presence of different types of FRP components, in influencing the load response and compression behavior of the piles.

The comparison of static loading behavior before and after cyclic loading tests can be made to investigate the effect of cyclic loading history on pile body (Fig. 9) and shaft resistance (Fig. 10) development. Generally, Pile 2 showed no significant change in the strength development under static loading after 120-90 cyclic loading was applied, indicating that the pile capacity almost kept stable when cyclic loading was within a certain threshold. However, after 180-60 cyclic loading was applied, the strength mobilization rate of Pile 2 degraded, as shown in Fig. 9(a). On the contrary, Pile 3 started to degrade after 120-90 cyclic loading was applied (Fig. 9(b)). This difference between Pile 2 and Pile 3 is due to the difference in confinement, which is also confirmed by the tangent modulus degradation, as shown in Fig. 8(b). Pile 4 generally showed less change after 60-60 cyclic loading was applied (Fig. 9(c)). As shown in Fig. 10, the deformation resistance in the rock socket kept improving with a cyclic loading level smaller than 120-90, while it kept almost stable when the cyclic loading level increased to 180-90. The detailed discussion on the deformation mechanism at the pile-rock interface will be presented in Sections 3.6 and 3.7.

3.2 Axial strain along depth of model piles

The axial strain profiles of Pile 2, Pile 3, and Pile 5 at different depths along the pile body under different monotonic load levels are shown in Figs. 11(a), 11(b), and 11(c), respectively. When the load level was lower than the ultimate value, the pile strain presented a generally similar pattern along the pile depth under different load levels, with a peak value at the depth of 340 mm and a minimum value at the level of the rock surface. The pile was equipped with a circular steel transferring case, as illustrated in Fig. 1, to facilitate uniform loading transfer from the loading actuator to the pile head. This circular steel casing had a length of 200 mm, encompassing the pile head, providing additional confinement, and creating a semi-fixed end condition for the pile head, in contrast to the fixed end condition at the pile bottom. Moreover, being a slender pile with a slenderness ratio of 14.5, the deformation of the pile could have been influenced by its slender nature, particularly in the form of bending or buckling. Considering the fixation conditions at both ends of the pile, the largest moment for all piles would occur at the position with the greatest bending, which was observed to be in the range of 300-400 mm just below the circular steel casing, as shown in Fig. 11.

The axial strain demonstrated a decreasing trend starting from the aforementioned position as the bending effects attenuated with depth until reaching the rotation center of the pile, which occurred within the range of 600-700 mm. For each pile, the axial strain experienced a slight increase as the pile depth increased within the range of 600-1000 mm for Pile 2 (Fig. 11(a)) and Pile 3 (Fig. 11(b)) and within the range of 600-800 mm for Pile 5 (Fig. 11(c)). This behavior can be attributed to the increasing bending effects from the rotation center toward the pile bottom. Consequently, Pile 2 and Pile 3, which were confined with an FRP tube or an FRP rebar cage, exhibited better ductility compared to Pile 5, which only had a central FRP rebar. The axial strain experienced a sharp decrease from a depth of 1150 mm due to a significant reduction in bending effects caused by the strong confinement provided by the rock socket, particularly pronounced from a depth of 1300 mm onwards. Notably, the sea sand seawater concrete (SSC) was poured directly into the GFRP tube or tubular mold from the pile head. This pouring method could have created a potential density gradient along the height of the pile. As a result, there might have been a higher density of SSC near the bottom of the pile and a lower density near the pile head. This density gradient could have led to an overall increase in stiffness with increasing pile depth, resulting in a general decrease in axial strain along the pile.

All the model piles failed at the same position, 0 ~ l_a /4, near the pile head on account of low-end fixity at the pile head, except for obvious damage between 0 ~ l_a/4 from the pile bottom in the case of Pile 3, as shown in Fig. 12. Pile 2 failed due to the rupture and buckling of the FRP tube shown in Fig. 12(a). It can be found from Fig. 12(b) that the rupture of longitudinal FRP rebars and cracks in the concrete cover led to spalling and the failure of Pile 3. Piles 4 and 5 failed due to the separation of concrete from FRP rebars and the breakage of FRP rebars, which resulted in brittle failure, as shown in Fig. 12(c).

3.3 Cyclic stiffness of pile body

The stiffness of a pile plays a crucial role in determining the load transfer mechanism and the distribution of strains along its length. The experimental results on pile stiffness can be used to validate and improve numerical models and theoretical predictions which can contribute to design of piles in the future. The cyclic stiffness of model piles was calculated by the following equation:

$$k_{cyc,pb} = 2\frac{Q_{cyc}}{u_{cyc,pb}} \tag{5}$$

where $k_{cyc,pb}$ represents the cyclic stiffness of the pile body above the rock socket determined in each cycle, and $u_{cyc,pb}$ refers to the recoverable deformation at the pile head when the peak load is released back to the valley value in the respective cycle. The deformation was calculated by integrating the strain measured with eight FBGs in the pile body (l_a), as shown in Eq. (4). The stiffness was calculated in the kN/mm unit in this study.

The variations in the $k_{cyc,pb}$ of Pile 2 under different cyclic loading conditions against cycle number are presented in Fig. 13. Stiffness increased almost linearly during the first loading (60-60) in the first series, as shown in Fig. 13(a). When the second loading of 120-60 was applied, the stiffness increased suddenly from 175 to 180, then degraded quickly in the initial 10 cycles, followed by a slight increasing trend till the 100th cycle under the loading. It can be observed that the pile showed higher stiffness under this intermediate loading (120-60) in all series, as shown in Figs. 13(a)-13(d) compared with the higher or lower loadings (120-90 and 60-60), attributed to a certain load threshold within which strain hardening occurs. The deformation of SSC, at this stage, is mainly contributed by elastic compression of aggregates and closure of micro cracks, which is enhanced by the confinement of the GFRP tube. As the load increased, the FRP tube underwent some fiber breakage or delamination due to cyclic loading (Schoeppner and Abrate, 2000; Pitarresi et al., 2019; He et al. 2021), the micro-cracks in SSC develop in size and propagate, and cementitious products exhibit plastic flow behavior, thereby reducing stiffness.

Note that the axial load was released to zero between two consecutive loading stages. Stiffness in the first three series generally increased with cycle number and stabilized during the fourth. It can be concluded that the pile body had adapted to the loading levels after several loading-unloading cycles were applied. On the other hand, the stiffness under each loading level kept increasing from Series 1 to Series 4. For example, the pile gained stiffness of up to 6% from the minimum 166 kN/mm in the first series to the maximum stiffness of 185 kN/mm in the fourth series for the 120-60 loading, indicating that the unloading-reloading cycle strengthened the deformation resistance of FRP tube confined concrete pile for which confinement action from the FRP tube was activated with the deformation accumulated. In Series 5, as shown in Fig. 13(e), under higher cyclic loading applied, the stiffness of Pile 2 achieved a large value of around 187 kN/mm, then degraded quickly within the initial 25 cycles and afterward stabilized at a level of 177.5 kN/mm, which is lower than that under 120-60 in first four series. Interestingly, the stiffness, however, still increased gradually with the loading sequence, which should be attributed mainly to the microstructure adjustment resulting from unloading-reloading cycles between each two consecutive loading cases and continuous enhancement in stiffness due to the confinement development of the FRP tube.

The stiffness variations of Pile 3 over cycles under different cyclic loading conditions are shown in Fig. 14. During the loading 60-60 in series 1, stiffness showed a stable trend. When the load was increased, however, a slowly increasing trend was observed in the first 30 cycles, followed by a stable behavior with cycle number for the first two 120-60 tests, as shown in Fig. 14(a). In contrast, degradation was marked in the first 12 cycles during the third 120-60 repeated test but reached a similar level of stiffness of Series 2 in the following cycles. For the same mean load and cyclic amplitude, the repeated tests resulted in gains of 5% in stiffness, which could be attributable to the strain-hardening effect. When cyclic amplitude was increased further in test 120-90, shown in Fig. 14(b), the pile showed less stiffness than in test 120-60. It can be possibly expected that If cycling would continue for the same test (120-90) or higher load, stiffness could presumably show a further decrease. Compared with the further increase trend of FRP tube confined concrete pile (Pile 2) under 180-60 loading, the FRP rebar cage showed a less confining enhancement effect on the pile. Then, the loading conditions were reduced back to investigate the effect of high loading history on the stiffness behavior of the pile body when subjected to subsequent lower cyclic loadings. As shown in Fig. 14(b), stiffness overall degraded from 162 kN/mm for 120-60 loading to 130 kN/mm for 60-30 loading. However, as shown in Fig. 14(c), a slight gain of stiffness was observed in the repeated tests 60-60 in Series 5 compared with that in Series 4. Combined with the results of Pile 2, the pile body preloaded by a higher loading around the strain hardening threshold would gain slightly in stiffness. The stiffness under 90-60 and 90-90 loadings laid between 60-60 and 120-60 cases, which possibly indicates that the maximum cyclic loadings (Q_{cyc}+Q_{mean}) are the main influencing factor for the cyclic stiffness, provided that the loading level is more or less within the strain hardening threshold.

The variations in the stiffness of Piles 4 and 5 under cyclic loadings with increasing cycle numbers are shown in Fig. 15. Initially, Pile 4 showed almost constant stiffness with the increase of cycle number under low-level cyclic loading 30-30. However, when the pile was unloaded and retested under increased loading conditions 60-60, stiffness degradation was observed in the first 50 cycles, followed by a constant stiffness trend. As a result of being reinforced with the centered FRP rebar of a high modulus of elasticity and high strength, the pile showed no significant change in stiffness. Additionally, Q_{cyc} and Q_{mean} were kept under 30 % of post-cyclic monotonic capacity Q_{ps}, which is below the load threshold capable of inducing the significant stiffness degradation of the pile. During the first cyclic loading 30-30 on Pile 5, stiffness showed an initial degradation of 3% in the first 40 cycles. Then, it linearly increased to the initial value at N = 108 and degraded again till 400 cycles, followed by a constant trend. This variation in stiffness can be attributed to the rearrangement and compaction of the slag under compression in the rock socket, destabilizing the behavior of the pile in the initial loading stage. During test 60-60, stiffness degraded slowly in the first 200 cycles, followed by a constant trend of nearly similar value 156 kN/mm as in the previous test 30-30 till N = 1,000. The cyclic loading tests on Piles 4 and 5 suggest that applying the maximum cyclic load (Q_{cyc} + Q_{mean}) below 35% of the post-cyclic capacity of the pile for 1,000 cycles may not significantly change the stiffness of the pile with a center-positioned FRP rebar. It can be observed that stiffnesses under cyclic loading (Figs. 13, 14, and 15) are generally greater than those under static loading (Fig. 8) when the loading level is similar, especially for Pile 2 and Pile 3. The possible reasons can be illustrated as follows: (a) the cyclic stiffness is calculated based on the recoverable deformation observed when a portion of the applied loading is released, which represents the elastic behavior of the pile; (b) the static stiffness observed during monotonic loading may be influenced by some unrecoverable strain resulting from microcracks and other defects within the pile; (c) cyclic loading can be considered a conditioning stage that aids in redistributing microcracks evenly throughout the concrete, achieving a more balanced state and facilitating the effective distribution of applied loads.

3.4 Accumulated compression of pile body during cyclic loading

The accumulated pile compression $u_{acc,pb}$ is the compression accumulated in the pile body over l_a from the first cycle to the last during cyclic loading. The accumulated compression of Pile 2 under different maximum cyclic loadings (Q_{cyc}+Q_{mean}) in different series is shown in Fig. 16. Compression accumulation was maximum during the first cyclic loading series, with a higher value of 200 μm observed in test 120-60. In the very first cyclic loading series, the conditioning of the pile may change and respond differently to cyclic loading. Each subsequent series from 1 to 3 showed a reduction in pile compression accumulation. However, a similar response was recorded during Series 3 and 4, which can be attributed to the effect of load history. During the cyclic loading tests 60-60, 120-60, and 120-90 from Series 1 to 4, compression accumulation was reduced by roughly 70%, 86%, and 67%, respectively, leading to the gains in stiffness observed in section

3.3. The pile accumulated the maximum compression of 400 μm during the first test (180-60) in Series 5. However, it exhibited a nearly 77% reduction in compression accumulation under the same loading conditions from the first to fourth tests in this series. Therefore, it is generally observed that cyclic loading history reduced compression accumulation for the following loading stages with the same cyclic loading conditions. As the main component to sustain compressive cyclic loading, SSC, in the initial loading conditions, contributes to the major compression accumulation due to the formation and distribution of microcracks. However, as the loading continues, the stresses are redistributed evenly across the concrete, achieving a balanced state, which helps to distribute the applied loads effectively, leading to a reduction in the rate of compression accumulation. Besides, the enhanced confinement from the FRP tube restrained SSC laterally and increased its deformation resistance by inhibiting damage propagation and crack growth in SSC (Lam and Teng, 2003). Hence, it was advisable to consider the effect of cyclic loading in ultimate state design when examining piles with competent confinement, like the FRP tube.

3.5 Cyclic stiffness and permanent accumulated compression of piles in rock socket section

Fig. 17 presents how the cyclic stiffness of the pile in the rock socket evolved under various cyclic loading conditions. In Series 1, stiffness increased linearly with the increase of cyclic loading at a slow rate. A higher cyclic stiffness of 8,915 kN/mm was recorded under 120-60 loading in Series 2 due to the strain hardening caused by the load within the threshold value, as discussed in Section 3.1. For each of test 60-60, 120-60, and 120-90 from Series 1 to 4, stiffness increased with cyclic loading, achieving gains of up to 4.3%, 8.4%, and 2.85%, respectively. Then, stiffness increased slowly under higher cyclic loading in Series 5, achieving gains of only 3.68% from 8,421 to 8,731 kN/mm with repeated testing. Based on the theoretical framework introduced by Manceau et al. (2021), the shaft resistance is governed mainly by the rock socket roughness, shear modulus of rock, and pile diameter. Initially, small gaps between asperities of rock and pile shaft may have existed. As the cyclic loading continued, dilation at the rock-pile interface developed, leading to an increase in normal stress, which induced a higher cyclic stiffness. However, when the load increased and the cycle number accumulated, partial wear and damage of asperities contacts between rock and pile occurred, which reduced the dilation and normal stress at the interface. With the further increase of loading, the debris from asperity fracture would be compressed again, thereby inducing denser packing and dilation. Since the shaft resistance has a negative correlation with pile diameter (Manceau et al., 2021), the effect of external loading on the shaft resistance behavior would be less obvious for the large-diameter piles. Therefore, precautions should be taken when applying the observed trends in practical design. The total accumulation of compression in the pile socket as a consequence of a series of cyclic loadings is presented in Fig. 18. Compression accumulated at a high rate with the increase of loading, whose accumulation, however, was less marked on retesting in the following series due to the gains in stiffness, and a total of 12 μm permanent compression accumulated within the socket as a result of cyclic loading from Series 1 to the end of series 5. The high strength of the rock resulted in less compression within the rock socket compared with that within the pile body.

3.6 Compression of the pile section in the rock socket during cyclic loading

In this section, the compression of the piles within the rock socket under static loading (Q_{mean}) before cyclic loading and post-cyclic stages was analyzed. The variation in the compression of the pile in the socket when it was subjected to static and cyclic loadings is presented in Fig. 19. The compression under static loading showed a linear response with the increase of load magnitude. Under the same static loads of 60 and 120 kN in each series, compression was kept nearly constant for each test with a value of 8 and 16 μm, respectively. At a higher static load of 180 kN in Series 5, compression increased linearly to 23 μm and showed no obvious change during the retests in the same series.

The compression of the socketed section of the pile after cyclic loading showed a different phenomenon. As shown in Fig. 19, the compression accumulation under cyclic loading evolved at a slower rate compared with that under static loading, explained by the repetitive shearing dilation at the rock-concrete interface due to the increased confinement resulting from the breakage of interface asperities and their rearrangements, corresponding to the theoretical framework proposed by Manceau et al. (2021) and their field test results of drilled and grouted piles in rock. Within the first series, the socket deformed more than other series under the same loading conditions and showed a high compression of 17.7 μm under 120-60 loading within Series 1 to 4. Compression was kept almost constant for each respective test in Series 2, 3, and 4 as the results of the conditioning effect of cyclic loading in Series 1. Moreover, it experienced a maximum compression of 25 μm under higher cyclic loading of 180-60. However, it increased at a lower rate under the same loading conditions in subsequent tests due to the cyclic conditioning effect from prior loadings.

3.7 Mobilization of shaft friction under cyclic loadings

The shaft friction *f* inside the rock socket between the granite rock and the pile was measured from the load distribution in the pile body inside the socket. The load distribution was calculated from the distributed strain data of pile measured with OFDR optic fibers rather than FBG. As a discrete sensing element, the FBG adopted in this study has a length of 15 mm, which indicates it will measure the average strain within this range. However, one of the FBG sensors in the pile was located at the level of the rock surface such that the stuck effect, induced by the imperfect matching between the pile and the drilled socket hole, would affect the accuracy of that specific FBG sensor. On the other hand, OFDR provides a more detailed profile of shaft friction along socket depth due to its full distribution nature. Rock quality designation (RQD) was kept the same for all the model piles. Piles 4 and 5 were not instrumented with OFDR optic fibers, and OFDR optic fibers in Pile 2 could not provide data along the entire socket length. Hence, the shaft friction results of Pile 3 were discussed as a representative pile. The following relation was used to calculate the shaft resistance in the rock socket:

$$f = \frac{\Delta F}{\Delta h.\pi.D} = \frac{\Delta\sigma_c A_c + \Delta\sigma_f A_f}{\Delta h.\pi.D} \tag{6}$$

where Δh is the distance between the two sensing points, D represents pile diameter, and A_c and A_f denote the cross-section areas of concrete and FRP rebars, respectively. For Pile 3, four GFRP rebars, along with the SSC, were placed in the rock socket. To calculate the axial stress σ_c of concrete, the tangent modulus E_t discussed in Section 2.2 was adopted by considering concrete as a non-linear elastic-plastic material. FRP was treated as an elastic material, and the incremental axial stress along the depth was calculated as $\Delta\sigma_f = \Delta\varepsilon E_f A_f$, where E_f is the modulus of FRP.

The variations of mobilized shaft friction f and displacement along the depth in the rock socket at cycles N = 3, 25, 50, and 100 in different cyclic loading tests are shown in Fig. 20. The displacement in the socket was calculated as the change of longitudinal distance of each point relative to the point near the rock surface. It was observed that the behavior of mobilized rock shaft friction was non-linear, with some fluctuations along the depth in the socket. Shaft resistance evolved with cycles, showing gains of up to 15% from $N = 3$ to $N = 100$ at a socket depth of 10 mm for 60-60 loading in Series 1. The increase in shaft friction attenuated with the increase in depth, with almost no significant change to the pile base. Following a smooth curve with a maximum displacement of 3 μm in the region 0-20 mm, displacement decreased non-linearly along the depth and showed a nearly similar trend with cycles. For the 120-60 loading, as shown in Fig. 20(b), the mobilized shaft friction decreased generally with depth. Notably, the ratio of shaft friction at 10 mm depth under 120-60 loading and 60-60 loading was 2.5, while the ratio decreased to 1.88 at the pile base.

Compared with the previous test, 60-60, displacement increased with cycles, rising from 5.8 to 7 μm at $N = 100$. The maximum shaft friction of 4.6 MPa was observed at $N = 100$ under test 120-90 (Fig. 20(c)). Generally, shaft resistance increased with an increase in $Q_{cyc} + Q_{mean}$. However, when $Q_{cyc} + Q_{mean}$ increased by 10% from the 120-60 case to the 120-90 case, the maximum shaft friction increased by 23%. Moreover, the shaft frictions at the depths of 90 mm and 110 mm showed no difference for these two loading cases. The shaft frictions at 130 mm and 145 mm were even smaller for the 120-90 case. It can be speculated that the pile-rock interface at the upper portion mobilized largely with significant asperities breakage and an obvious increase in confinement from rock to pile due to the dilation effect of broken-out small particles. The magnitude changed less markedly with cycles in the lower section of the rock socket but increased with an increase in cycle number at the upper portion.

3.8 Mean shaft friction and end bearing under static loading

The axial load of piles ended in a rock socket is supported by combined shaft resistance and base resistance. The ultimate post-cyclic static monotonic load capacity Q_{us} of each model pile is shown in Table 5. For all the piles, the failures were observed in the pile body above the rock socket, indicating the higher pile capacity within the rock socket. The mean shaft friction, end bearing, and the load percentage taken by the shaft and base in the rock socket against the applied load are presented in Fig. 21(a). The mean shaft friction increased almost linearly with the increase in load; however, the end bearing showed a non-linear response. Around 78.4-88.9 % of the load was resisted by the pile shaft, and 11.1-21.6 % was resisted by the pile base, showing the major contribution by shaft resistance, corresponding to a ratio of shaft resistance over total loading of around 10% based on the design chart provided by Pells and Turner (1979). When the applied load was increased beyond 20 kN, the percentage contributed by shaft resistance decreased gradually while that of base increased. The contributions of shaft and base resistance against the displacement of the pile at the top cross-section of the rock socket are shown in Fig. 21(b). The shaft resistance mobilized at a small relative displacement between the rock and pile; hence, a significant portion of the applied load on rock-socked piles was transferred to the rock-pile interface at the side. It can be observed that when the displacement exceeded 3 μm, the pile base resistance started to mobilize and increased with the increase in applied load. Fig. 21(c) shows the variation of shaft friction along the socket under different static load levels. With the increase in load, the shaft friction increased, and the highest values were at the top of the socket and decreased downwards along the socket depth.

4 Conclusions

In this study, a series of physical model tests on rock-socketed FRP composite SSC model piles with different configurations under various axial cyclic loadings were reported. FBG and OFDR sensing technologies were used for measuring the strain profile within model piles to investigate strain distribution, axial cyclic stiffness, and shaft friction mobilization between SSC and rock. The main findings are as follows:

(a) The strain distribution along the depth of piles showed a similar trend for the model piles, with higher strains recorded in the region (0 - $l_a/4$) from the pile head. The failure of FRP tube confined and centered FRP rebar-reinforced SSC piles happened within this region near the pile head. However, the FRP rebar cage reinforced SSC pile showed the maximum compression in the same region near the pile head and rock surface.

(b) FRP-SSC piles with a center FRP rebar exhibited the highest initial modulus in contrast to the piles with FRP tube or FRP stir-ups, while the former showed continuous strain softening and strain hardening for the latter ones with the increase of compression. The FRP tube confined pile showed higher ductility and capacity comparatively, suggesting the best solution for field applications in terms of mechanical performance.

(c) The pile body gained cyclic stiffness when the maximum cyclic load level ($Q_{mean} + Q_{cyc}$) was below 30% of Q_{us}, and degradation was observed under higher load conditions. The stiffness of the pile body showed gains of up to 5% for the mentioned load levels, with the maximum stiffness observed on the FRP tube confined pile. The cyclic stiffness of the socket section increased linearly with the increase in cyclic load levels due to the high modulus and strength of the rock.

(d) Both Q_{mean} and Q_{cyc} levels influenced the accumulation of compression, with the maximum compression accumulated within the pile body during test 120-60, around the threshold loading for the FRP tube confined pile.

(e) Shaft resistance in rock socket increased with (Q_{mean} + Q_{cyc}). The pile-rock interface at the upper portion mobilized largely with more significant asperities breakage and an obvious increase in confinement from rock to pile due to the dilation effect of broken-out small particles. The magnitude changed less markedly with cycles in the lower section of the rock socket but increased with an increase in cycle number at the upper portion.

The experiments provided the first systematic study to investigate the behavior of innovative and sustainable pile foundations, namely FRP composite SSC model piles ended in a rock socket under axial cyclic and static loadings. It should be emphasized that the scale effect should be carefully considered when generalizing the findings from physical model tests to practical projects, especially the pile-rock interface behavior. However, the results from physical model tests can be utilized to validate numerical approaches that could be taken to predict the behavior of full-scale piles in the field. Furthermore, it is necessary to perform additional experiments to investigate the effect of diverse cyclic loading parameters, shaft resistance from the surrounding soil, and the impact of combined lateral and vertical loadings on model piles in future studies.

Data Availability Statement

Some or all data, models, or codes that support the findings of this study are available from the corresponding author upon reasonable request.

Acknowledgments

The above research was funded by a Theme-based Research Scheme project (T22-502/18-R), a Research Impact Fund project (R5037-18), and two GRF projects (PolyU 15210020 and PolyU 15210322) from the Research Grants Council of Hong Kong Special Administrative Region Government of China, respectively. The authors of this work also gratefully acknowledge the financial support of the Research Institute of Land and Space of PolyU (CD82, CD7A) and the Research Centre for Resources Engineering towards Carbon Neutrality (BBEJ).

Notation

A_c	cross-sectional area of concrete
A_f	cross-sectional area of FRP rebars
c_1	strain coefficient
c_2	temperature coefficient
C_ε	strain coefficient
C_T	temperature coefficient
D	pile diameter
E_c	elastic modulus of concrete
E_f	elastic modulus of FRP rebar
E	young’s modulus
E_t	tangent modulus
f	shaft resistance
f_{cm}	peak stress
ΔF	change in axial force
Δh	distance between the two sensing points

i	initial state
l_a	length of pile from pile head to rock surface
$k_{cyc,pb}$	cyclic stiffness of the pile body above the rock socket
N	number of cycles
n	scale factor
Q_{cyc}	axial cyclic amplitude
$Q_{\max}$	maximum cyclic load
Q_{mean}	mean axial cyclic load
Q_{min}	minimum cyclic load
Q_{us}	post cyclic compression capacity
ΔT	temperature change
UCS	unconfined compressive strength
$u_{cyc,pb}$	change in the compression of the pile body in the respective cycle
u_{pb}	pile body compression
z	depth below pile head
ε_c	axial strain
ε_{cm}	strain at peak stress
$\varepsilon(z)$	strain at depth below pile head
η	ratio of axial strain to strain at peak stress
σ_c	axial stress of concrete
$\Delta\sigma_c$	change in axial stress of concrete
$\Delta\sigma_f$	change in axial stress of FRP rebars
$\Delta\varepsilon$	strain change
$\Delta\nu$	Rayleigh spectrum
λ	reflected light wavelength
$\Delta\lambda$	change in wavelength
λ_i	initial wavelength

References

ASTM C 469-94, Test for Static Modulus of Elasticity and Poisson's Ratio of Concrete in Compression, ASTM, USA (2000)

Bekki, H., Canou, J., Tali, B., Dupla, J. C., & Bouafia, A. (2013). Evolution of local friction along a model pile shaft in a calibration chamber for a large number of loading cycles. Comptes Rendus Mécanique, 341(6), 499-507.

Buckley, R. M., Jardine, R. J., Kontoe, S., Parker, D., & Schroeder, F. C. (2018). Ageing and cyclic behaviour of axially loaded piles driven in chalk. Géotechnique, 68(2), 146-161.

Buildings Department Technical Committee of Hong Kong (BD). (2017). Code of Practice for Foundations 2017. of Hong Kong.

Carter, J., & Kulhawy, F. H. (1988). Analysis and design of drilled shaft foundations socketed into rock.

Chan, S.-F., & Hanna, T. H. (1980). Repeated loading on single piles in sand. Journal of the Geotechnical Engineering Division, 106(2), 171-188.

Chen, W. B., Feng, W. Q., Yin, J. H., & Borana, L. (2020a). LVDTs-based Radial Strain Measurement System for Static and Cyclic Behavior of Geomaterials. Measurement, 155, 107526.

Chen, W. B., Feng, W. Q., Yin, J. H., & Qin, J. Q. (2021b). New fiber Bragg grating (FBG)-based device for measuring small and large radial strains in triaxial apparatus. Canadian Geotechnical Journal, 58(7), 1059-1063.

Chen, W. B., Liu, K., Yin, Z. Y., & Yin, J. H. (2020b). Crushing and flooding effects on one-dimensional time-dependent behaviors of a granular soil. International Journal of Geomechanics, 20(2), 04019156.

Chen, Z., Chen, W.-B., Yin, J.-H., & Malik, N. (2021a). Shaft Friction Characteristics of Two FRP Seawater Sea–Sand Concrete Piles in a Rock Socket with or without Debris. International Journal of Geomechanics, 21(7), 06021015.

Code, C.-F. M. (1990). CEB-FIP model code for concrete structures, euro-international committe for concrete. Bulletin(213/214).

Copsey, J., Hulme, T., Kraft, B., & Sripathy, P. (1989). Singapore mass rapid transit system: design. Proceedings of the Institution of Civil Engineers, 86(4), 667-707.

El Sharnouby, M. M., & El Naggar, M. H. (2012). Axial monotonic and cyclic performance of fibre-reinforced polymer (FRP) – steel fibre–reinforced helical pulldown micropiles (FRP-RHPM). Canadian Geotechnical Journal, 49(12), 1378-1392.

Fam, A., Flisak, B., & Rizkalla, S. (2003). Experimental and analytical modeling of concrete-filled FRP tubes subjected to combined bending and axial loads. ACI Struct. J, 100(4), 499-509.

Haberfield, C., & Collingwood, B. (2006). Rock-socketed pile design and construction: a better way? Proceedings of the Institution of Civil Engineers-Geotechnical Engineering, 159(3), 207-217.

He, H., Chen, W., Yin, Z., Kostas, K., & Yin, J. (2021). A micromechanical-based study on the tribological and creep-relaxation behavior of sand-FRP composite interfaces. Composite Structures, 275, 114423.

Hong, C., Wang, X., Han, K., Su, D., & Chen, Z. (2022). Performance investigation of 3D printed clay soil using fiber Bragg grating technology. Acta Geotechnica, 17(2), 453-462.

Horvath, R., Kenney, T., & Kozicki, P. (1983). Methods of improving the performance of drilled piers in weak rock. Canadian Geotechnical Journal, 20(4), 758-772.

Jardine, R., Zhu, B., Foray, P., & Yang, Z. (2013). Interpretation of stress measurements made around closed-ended displacement piles in sand. Géotechnique, 63(8), 613-627.

Jardine, R. J., & Standing, J. R. (2012). Field axial cyclic loading experiments on piles driven in sand. Soils and Foundations, 52(4), 723-736.

Jardine, R. J., Standing, J. R., & Chow, F. C. (2006). Some observations of the effects of time on the capacity of piles driven in sand. Géotechnique, 56(4), 227-244.

Juran, I., & Komornik, U. (2006). Behavior of fiber-reinforced polymer composite piles under vertical loads.

Klapper, J., Manceau, S., Hall, A., Jardine, R.J. and Barbosa-Moreira, P. (2020) The field behaviour of drilled and grouted piles in rock for offshore foundations. Proc. International Symposium on Frontiers in Offshore Geotechnics (ISFOG) 2022, Austin, Texas. Published ASCE DFI.

Krauss, P. D., & Nmai, C. K. (1996). Preliminary corrosion investigation of prestressed concrete piles in a marine environment: Deerfield beach fishing pier. ASTM special technical publication, 1276, 161-172.

Kulhawy, F. H., & Phoon, K.-K. (1993). Drilled shaft side resistance in clay soil to rock. Design and performance of deep foundations: Piles and piers in soil and soft rock,

Lam, L., & Teng, J. G. (2003). Design-oriented stress–strain model for FRP-confined concrete. Construction and Building Materials, 17(6-7), 471-489.

Li, Y., Zhao, X., & Raman, R. S. (2018). Mechanical properties of seawater and sea sand concrete-filled FRP tubes in artificial seawater. Construction and Building Materials, 191, 977-993.

Le Kouby, A., Canou, J., & Dupla, J. (2004). Behaviour of model piles subjected to cyclic axial loading. Cyclic behaviour of soils and liquefaction phenomena, 159-166.

Lin, S.-Q., Tan, D.-Y., Yin, J.-H., & Li, H. (2021). A Novel Approach to Surface Strain Measurement for Cylindrical Rock Specimens Under Uniaxial Compression Using Distributed Fibre Optic Sensor Technology. Rock Mechanics and Rock Engineering, 54(12), 6605-6619.

Manceau, S., Klapper, J., Jardine, R., Hall, A., & Barbosa Moreira, P. (2021). The Field Behaviour of Drilled and grouted piles in rock. Piling 2020: Proceedings of the Piling 2020 Conference.

McVay, M., Townsend, F., & Williams, R. (1992). Design of socketed drilled shafts in limestone. Journal of Geotechnical Engineering, 118(10), 1626-1637.

Mirmiran, A., Shahawy, M., & Samaan, M. (1999). Strength and ductility of hybrid FRP-concrete beam-columns. Journal of structural engineering, 125(10), 1085-1093.

Ng, C. W., Yau, T. L., Li, J. H., & Tang, W. H. (2001). Side resistance of large diameter bored piles socketed into decomposed rocks. Journal of Geotechnical and Geoenvironmental Engineering, 127(8), 642-657.

Nolan, S., Rossini, M., Knight, C., & Nanni, A. (2021). New directions for reinforced concrete coastal structures. Journal of Infrastructure Preservation and Resilience, 2(1), 1-12.

O'Neill, M. W., & Hassan, K. M. (1993). Perimeter load transfer in drilled shafts in the Eagle Ford formation. Design and Performance of Deep Foundations: Piles and Piers in Soil and Soft Rock,

Palmieri, L., & Schenato, L. (2013). Distributed optical fiber sensing based on Rayleigh scattering. The Open Optics Journal, 7(1).

Pando, M. A., Ealy, C. D., Filz, G. M., Lesko, J., & Hoppe, E. (2006). A laboratory and field study of composite piles for bridge substructures.

Park, J.-H., Jo, B.-W., Yoon, S.-J., & Park, S.-K. (2011). Experimental investigation on the structural behavior of concrete filled FRP tubes with/without steel re-bar. KSCE Journal of Civil Engineering, 15(2), 337-345.

Pells, P., & Turner, R. (1979). Elastic solutions for the design and analysis of rock-socketed piles. Canadian Geotechnical Journal, 16(3), 481-487.

Pitarresi, G., Scalici, T., Dellaira, M., & Catalanotti, G. (2019). A methodology for the rapid characterization of Mode II delamination fatigue threshold in FRP composites. Engineering Fracture Mechanics, 220, 106629.

Puech, A. (2013). 'Design for cyclic loading: piles and other foundations'. Proceedings of TC 209 workshop.

Rimoy, S. P., Jardine, R. J., & Standing, J. R. (2013). Displacement response to axial cycling of piles driven in sand. Proceedings of the Institution of Civil Engineers - Geotechnical Engineering, 166(2), 131-146.

Rowe, R., & Armitage, H. (1987). A design method for drilled piers in soft rock. Canadian Geotechnical Journal, 24(1), 126-142.

Sakr, M., Naggar, M. H. E., & Nehdi, M. (2004). Novel toe driving for thin-walled piles and performance of fiberglass-reinforced polymer (FRP) pile segments. Canadian Geotechnical Journal, 41(2), 313-325.

Sargin, M., & Handa, V. (1969). A general formulation for the stress-strain properties of concrete. SM Report Solid Mechanics Division, University of Waterloo, Canada(3).

Schoeppner, G. A., & Abrate, S. (2000). Delamination threshold loads for low velocity impact on composite laminates. Composites Part A: applied science and manufacturing, 31(9), 903-915.

Seidel, J., & Collingwood, B. (2001). A new socket roughness factor for prediction of rock socket shaft resistance. Canadian Geotechnical Journal, 38(1), 138-153.

Song, H., & Pei, H. (2022). A Nonlinear Softening Load-Transfer Approach for the Thermomechanical Analysis of Energy Piles. International Journal of Geomechanics, 22(5), 04022044.

Sze, J. W. (2015). Deep Foundations for High-Rise Buildings in Hong Kong. International Journal of High-Rise Buildings, 4(4), 261-270.

Tomblin, J., & Barbero, E. (1994). Local buckling experiments on FRP columns. Thin-Walled Structures, 18(2), 97-116.

Tsuha, C. d. H. C., Foray, P. Y., Jardine, R. J., Yang, Z. X., Silva, M., & Rimoy, S. (2012). Behaviour of displacement piles in sand under cyclic axial loading. Soils and Foundations, 52(3), 393-410.

Williams, A., & Pells, P. (1981). Side resistance rock sockets in sandstone, mudstone, and shale. Canadian Geotechnical Journal, 18(4), 502-513.

Wu, J., Liu, H., Yang, P., Tang, B., & Wei, G. (2020). Quantitative strain measurement and crack opening estimate in concrete structures based on OFDR technology. Optical Fiber Technology, 60, 102354.

Wu, P. C., Chen, W. B., Yin, J. H., Pan, Y., Lou, K., & Feng, W. Q. (2022). A Novel Sensor for Undrained Shear Strength Measurement in Very Soft to Soft Marine Sediments Based on Optical Frequency Domain Reflectometry Technology. Sensors, 22(15), 5530

Xiao, J., Qiang, C., Nanni, A., & Zhang, K. (2017). Use of sea-sand and seawater in concrete construction: Current status and future opportunities. Construction and Building Materials, 155, 1101-1111.

Zhan, C., & Yin, J.-H. (2000). Field static load tests on drilled shaft founded on or socketed into rock. Canadian Geotechnical Journal, 37(6), 1283-1294.

Zhang, B.-j., Huang, B., Mei, C., Fu, X.-d., Luo, G., & Yang, Z.-j. (2016). Dynamic behaviours of a single soft rock-socketed shaft subjected to axial cyclic loading. Advances in Materials Science and Engineering, 2016.

Zyka, K., & Mohajerani, A. (2016). Composite piles: A review. Construction and Building Materials, 107, 394-410.

Table 1. Similarity index of the physical model system

Physical parameter	Dimension	Model/ Prototype
Diameter of pile	L	1 / *n*
Length of pile	L	1 / *n*
Area	L^2	$1/ n^2$
Displacement	L	1/ *n*
Axial force	MLT^{-2}	$1/ n^2$
Strength	$ML^{-1}T^{-2}$	1
Young’s modulus	$ML^{-1}T^{-2}$	1
Shear modulus	$ML^{-1}T^{-2}$	1

Table 2. Mix design of SSC

Cement	Fly ash	Seawater	Sea-sand	Superplasticizer
0.75	0.25	0.6	3.25	0.013

Table 3. Chemical compositions of natural seawater in Chek Lap Kok, Hong Kong

Ion	Cl^-	Br^-	SO_4^{2-}	Li^+	Na^+	K^+	Mg^{2+}	Ca^{2+}	Salinity
(g/L)	18.153	0.066	1.675	0.0007	10.419	0.354	1.215	0.358	32.24

Table 4. Details of configuration, materials, and instrumentation of five model piles

Model Piles	**Pile Configuration**	**Materials**	**Instrumentation**	**Length**
Pile 1	FRP tube confined SSC pile	GFRP tube and SSC	FBG and OFDR sensors, LVDTs	Total 1460 mm (160 mm within granite rock socket and 1300 mm above rock surface)
Pile 2	FRP tube confined SSC pile	GFRP tube and SSC	FBG and OFDR sensors, LVDTs	
Pile 3	FRP rebar cage reinforced SSC pile	GFRP rebars, stirrups, and SSC	FBG and OFDR sensors, LVDTs	
Pile 4	Centered FRP rebar reinforced SSC pile	GFRP rebar and SSC	FBG sensors, LVDTs	
Pile 5	Centered FRP rebar reinforced SSC pile	GFRP rebar, SSC, and debris	FBG sensors, LVDTs	

Table 5. Cyclic loading program of the model piles

Model pile	Loading series	Test Code^1	Q_{mean} (kN)	Q_{cyc} (kN)	Cycle number, N	Loading frequency, f (Hz)	Post-cyclic failure load Q_{us} (kN)
Pile 1	-	60-60	60	30	100	0.01	-
		120-60	120	30	100		
		120-90	120	45	50		
		180-60	180	30	7^2		
Pile 2	Series 1	60-60	60	30	100	0.01	266
		120-60	120	30			
		120-90	120	45			
	Series 2	60-60	60	30			
		120-60	120	30			
		120-90	120	45			
	Series 3	60-60	60	30			
		120-60	120	30			
		120-90	120	45			
	Series 4	60-60	60	30			
		120-60	120	30			
		120-90	120	45			
	Series 5	180-60-1	180	30			
		180-60-2	180	30			
		180-60-3	180	30			
		180-60-4	180	30			
Pile 3	Series 1	60-60	60	30	100	0.01	213
	Series 2	120-60-1	120	30			
		120-60-2	120	30			
		120-60-3	120	30			
	Series 3	120-90-1	120	45	57		
		120-90-2	120	45			
	Series 4	60-30-1	60	15	100		
		60-30-2	60	15			
		60-30-3	60	15			
	Series 5	60-60-1	60	30			
		60-60-2	60	30			
	Series 6	90-60-1	90	30			
		90-60-2	90	30			

	Series 7	90-90	90	45	72		
Pile 4	-	30-30	30	15	1000	0.1	239
		60-60	60	30			
Pile 5	-	30-30	30	15	1000	0.1	208
		60-60	60	30			

Note 1. The first value represents Q_{mean}, second value refers to $2Q_{cyc}$, and if any third number, it represents the serial number of repeated tests within one series with respect to time (1 refers to the first test and so on).

Note 2. The pile failed unexpectedly due to the technical failure of the load transferring plate between the model pile and actuator during cyclic loading.

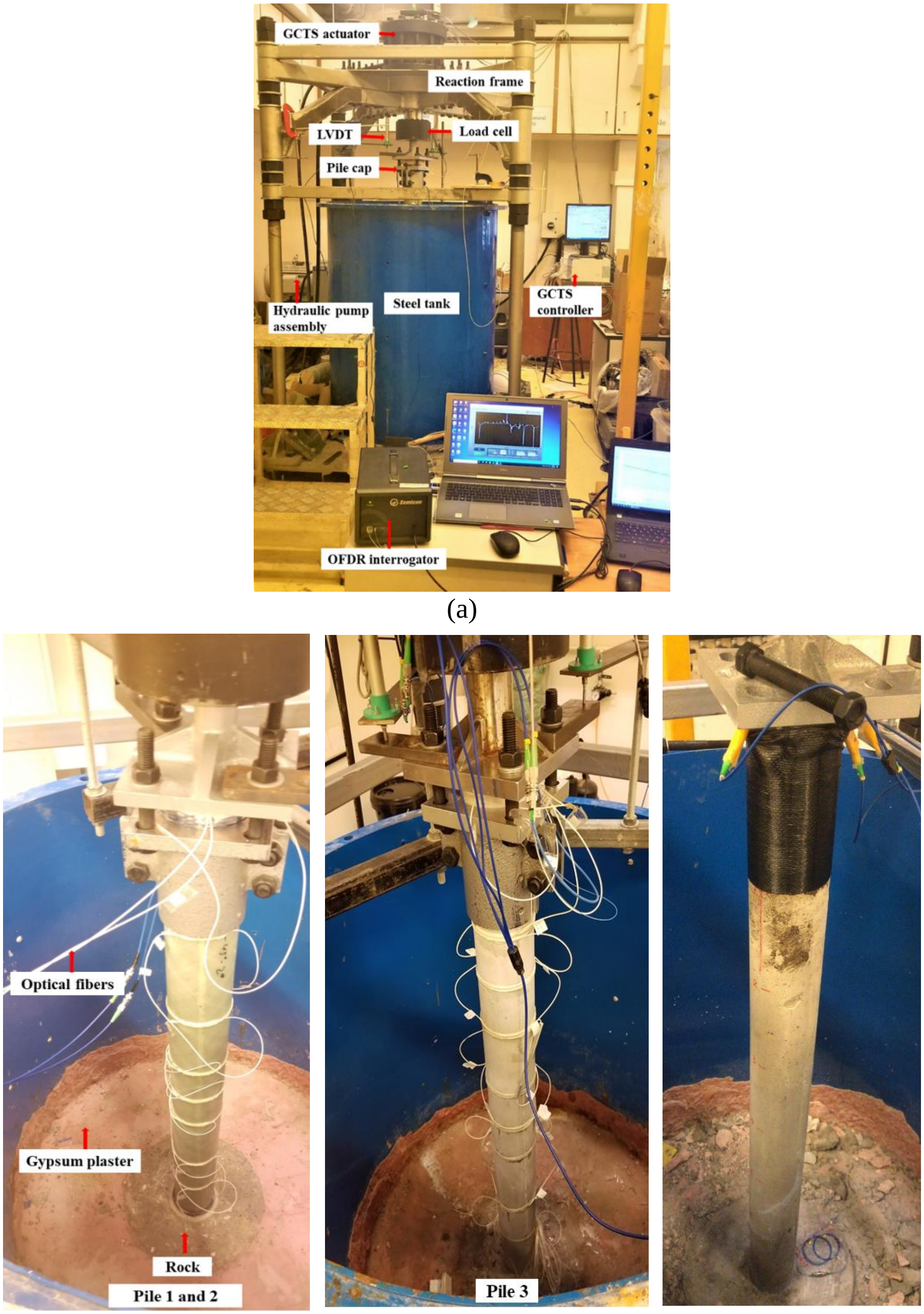

(a)

(b) (c) (d)

Fig. 1. Photos of the physical model system: (a) setup of the whole physical model system; (b) Pile 1 or Pile 2, (c) Pile 3, and (d) Pile 4 or Pile 5

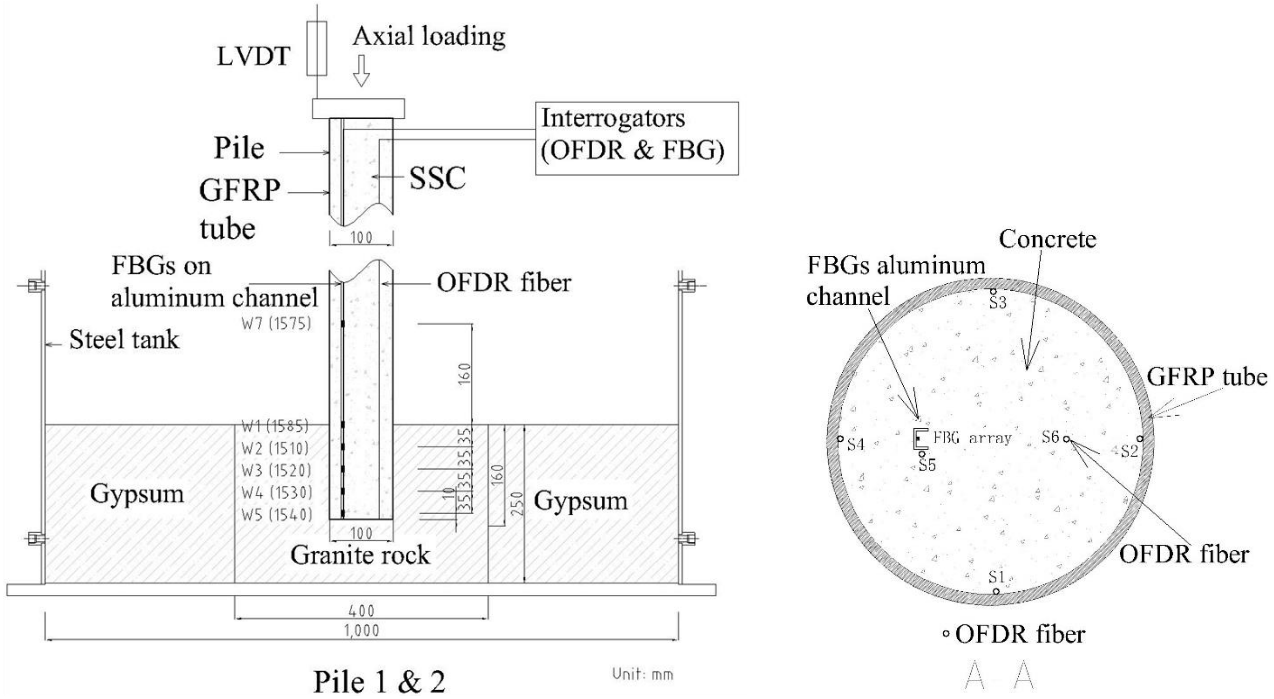

(a) (b)

Fig. 2. Cross-section illustrations of (a) vertical profile of Piles 1 and 2, and (b) horizontal profile of Piles 1 and 2

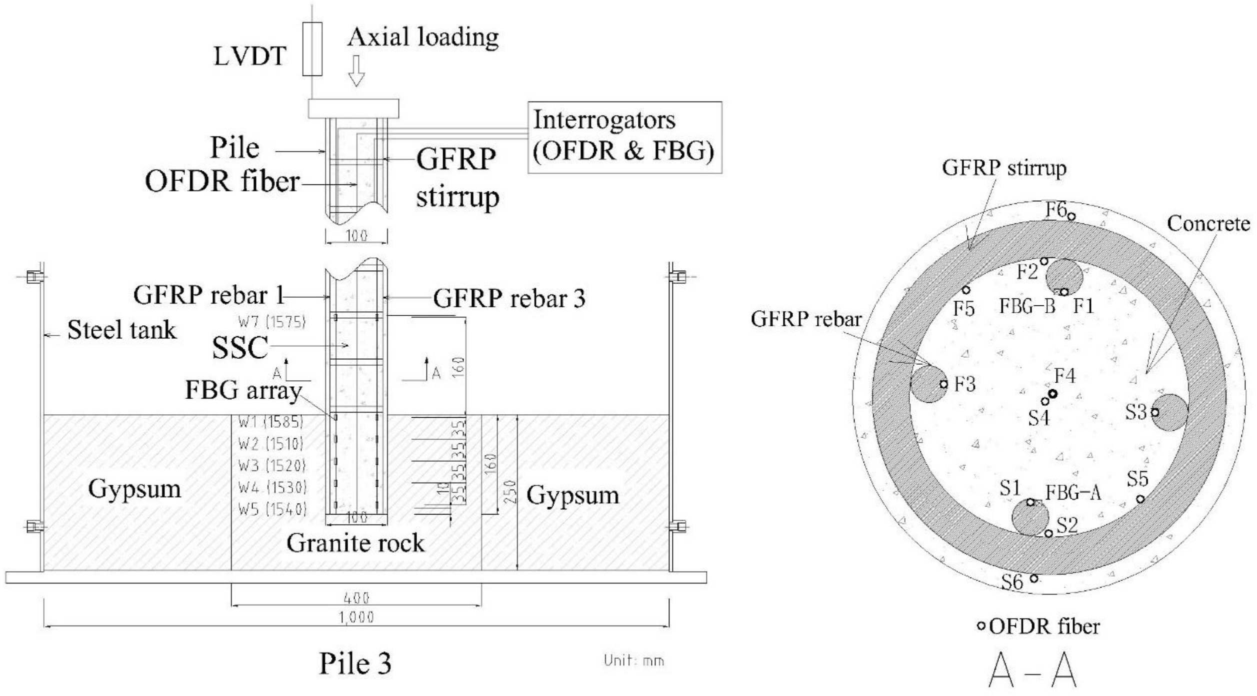

(a) (b)

Fig. 3. Cross-section illustrations of: (a) vertical profile of Pile 3, and (b) horizontal profile of Pile 3

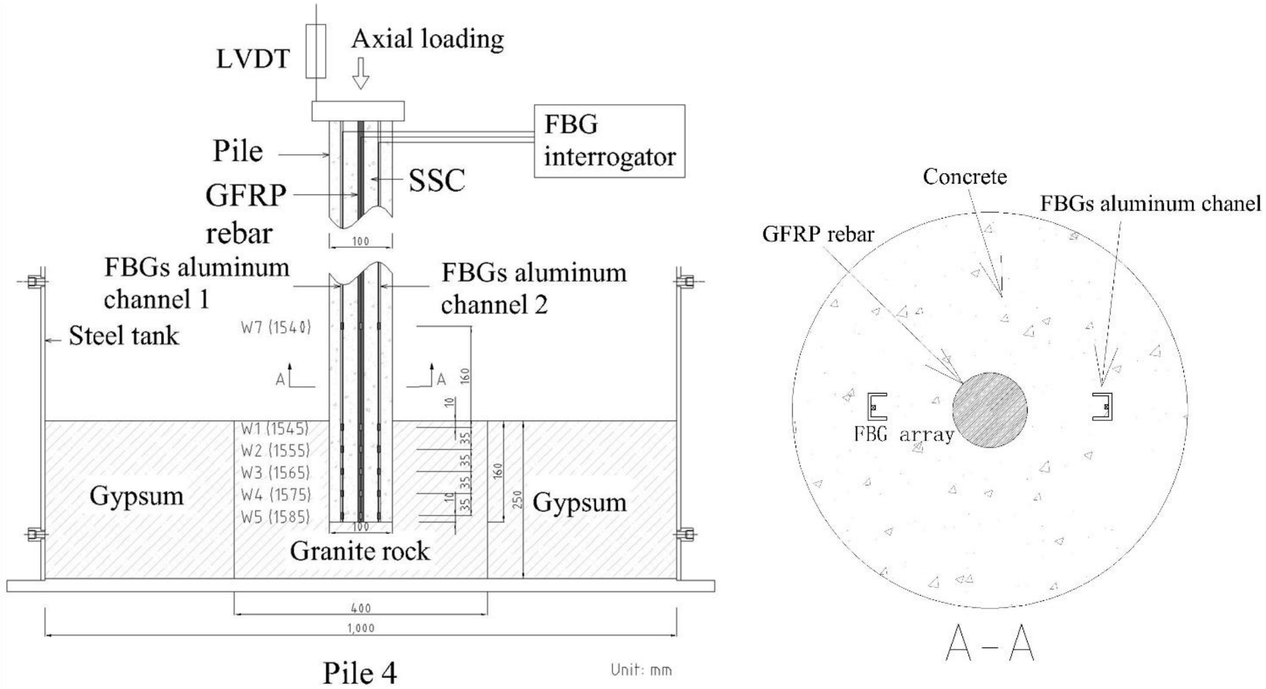

(a) (b)

Fig. 4. Cross-section illustrations of: (a) vertical profile of Pile 4, and (b) horizontal profile of Pile 4

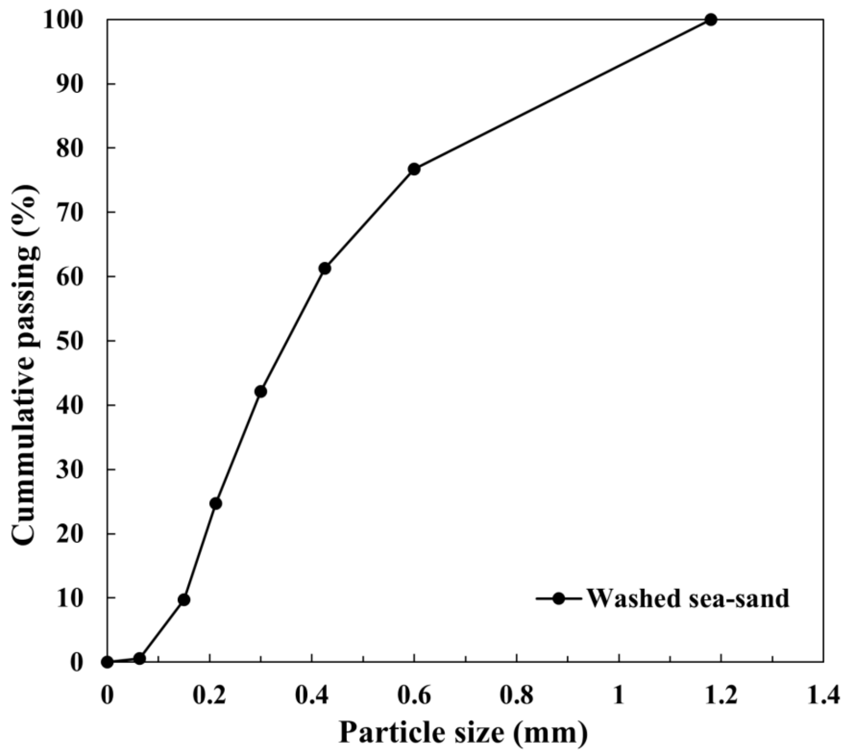

Fig 5. Particle size distribution curves of washed and unwashed sea-sand

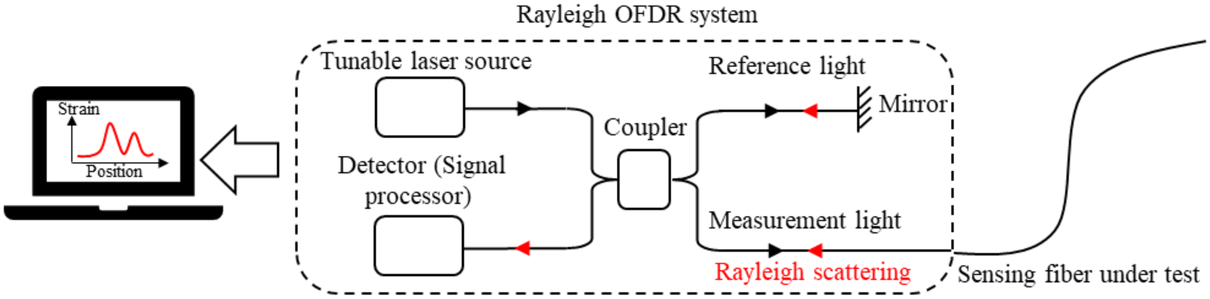

Fig. 6. OFDR sensing system

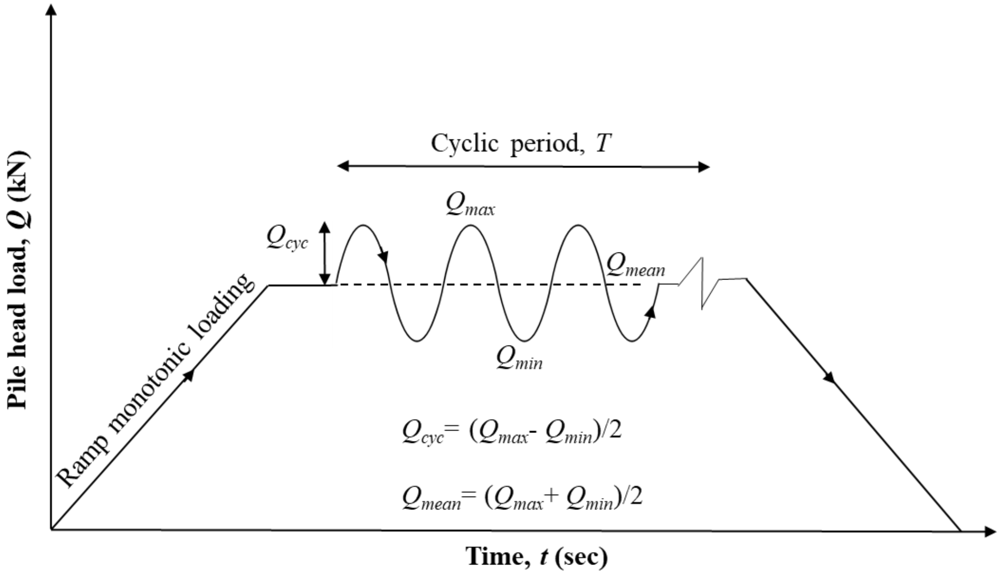

Fig. 7. Schematic illustration of loading program

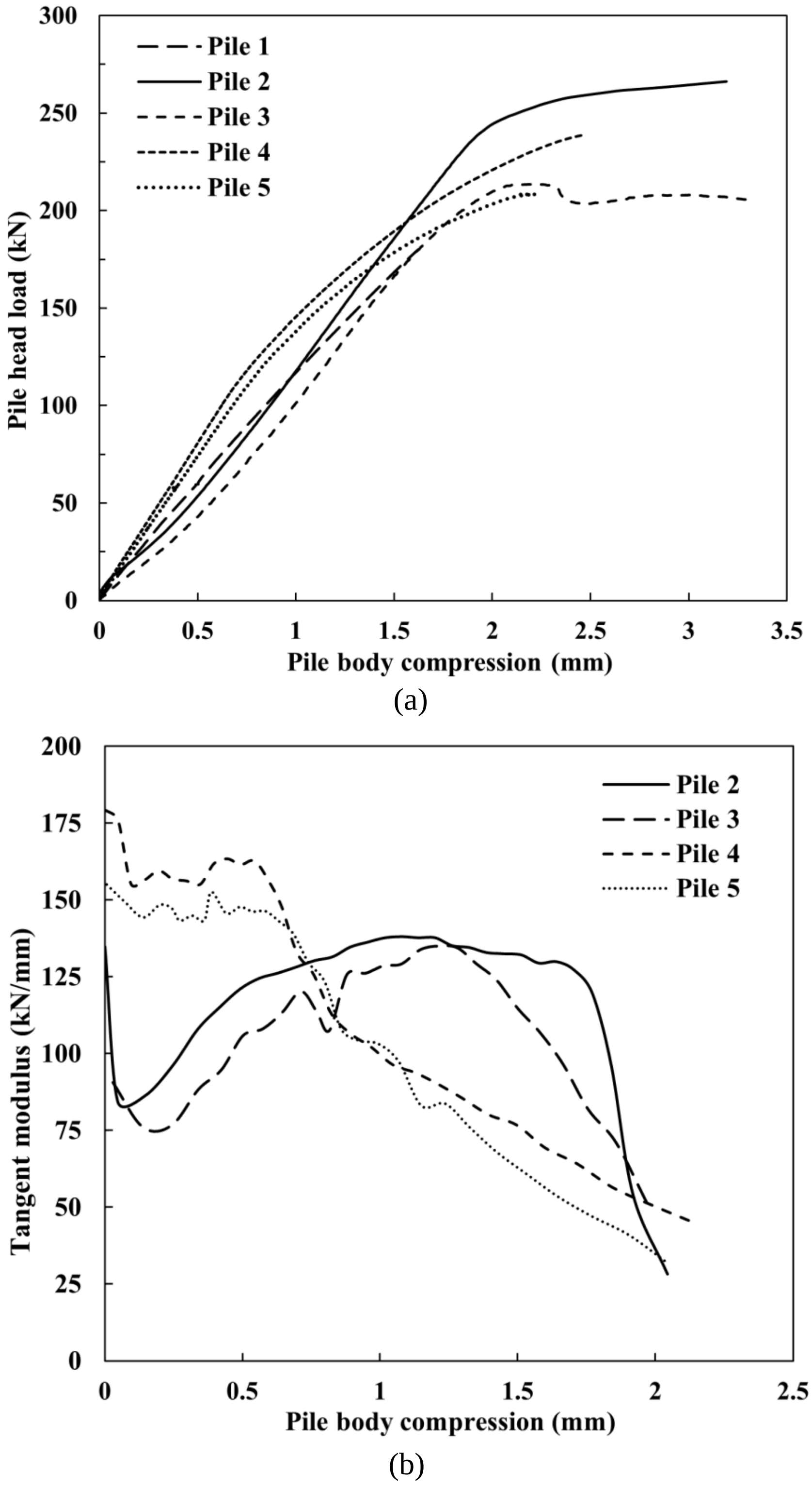

Fig. 8. (a) Static pile head load-pile body compression relationships of five FRP-SSC model piles, and (b) tangent modulus versus pile body compression of four FRP-SSC model piles

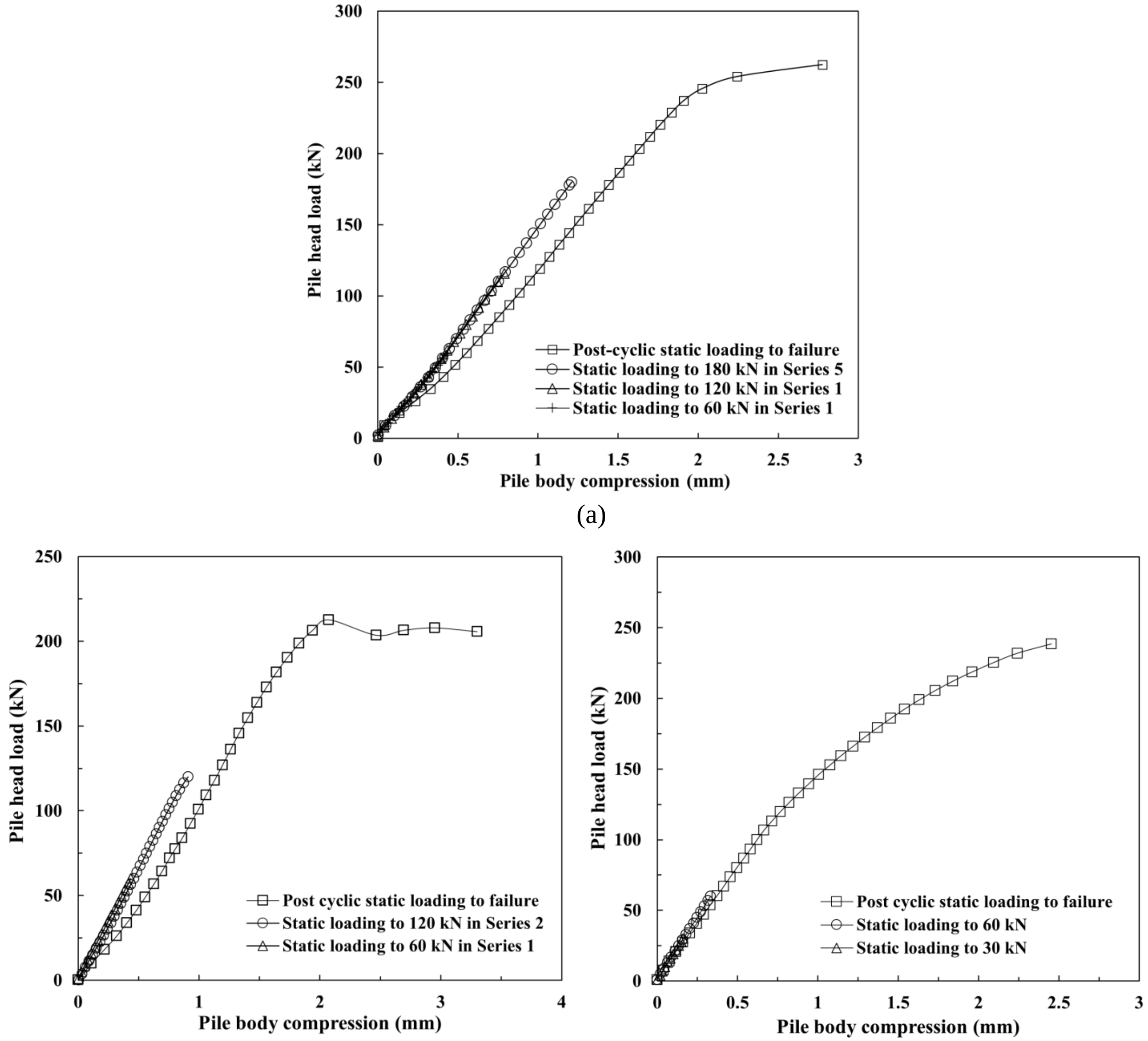

(a)

(b)

(c)

Fig. 9. Static pile head load-pile body compression relationships of (a) Pile 2, (b) Pile 3, and (c) Pile 4 before and after maximum cyclic loading

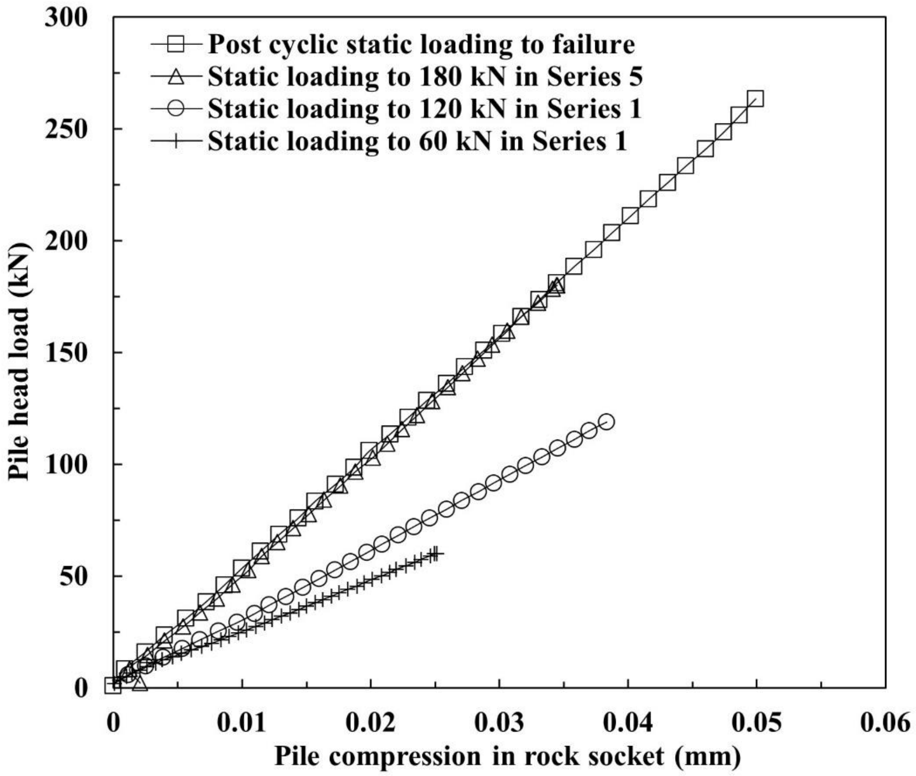

Fig. 10. Static pile head load-pile compression in rock socket relationships before and after maximum cyclic loading

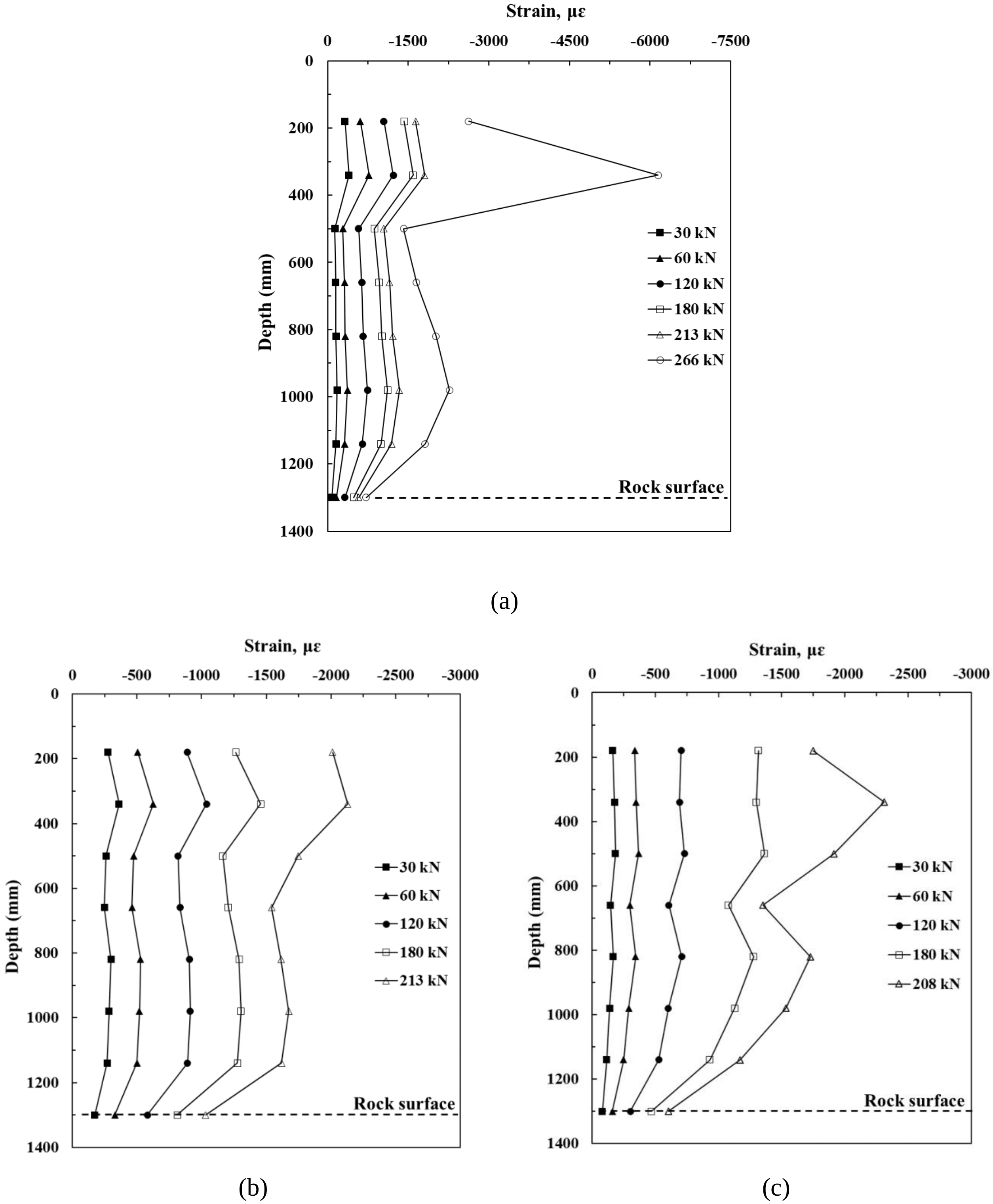

Fig. 11. Strain distribution along the depth of (a) Pile 2, (b) Pile 3, and (c) Pile 5

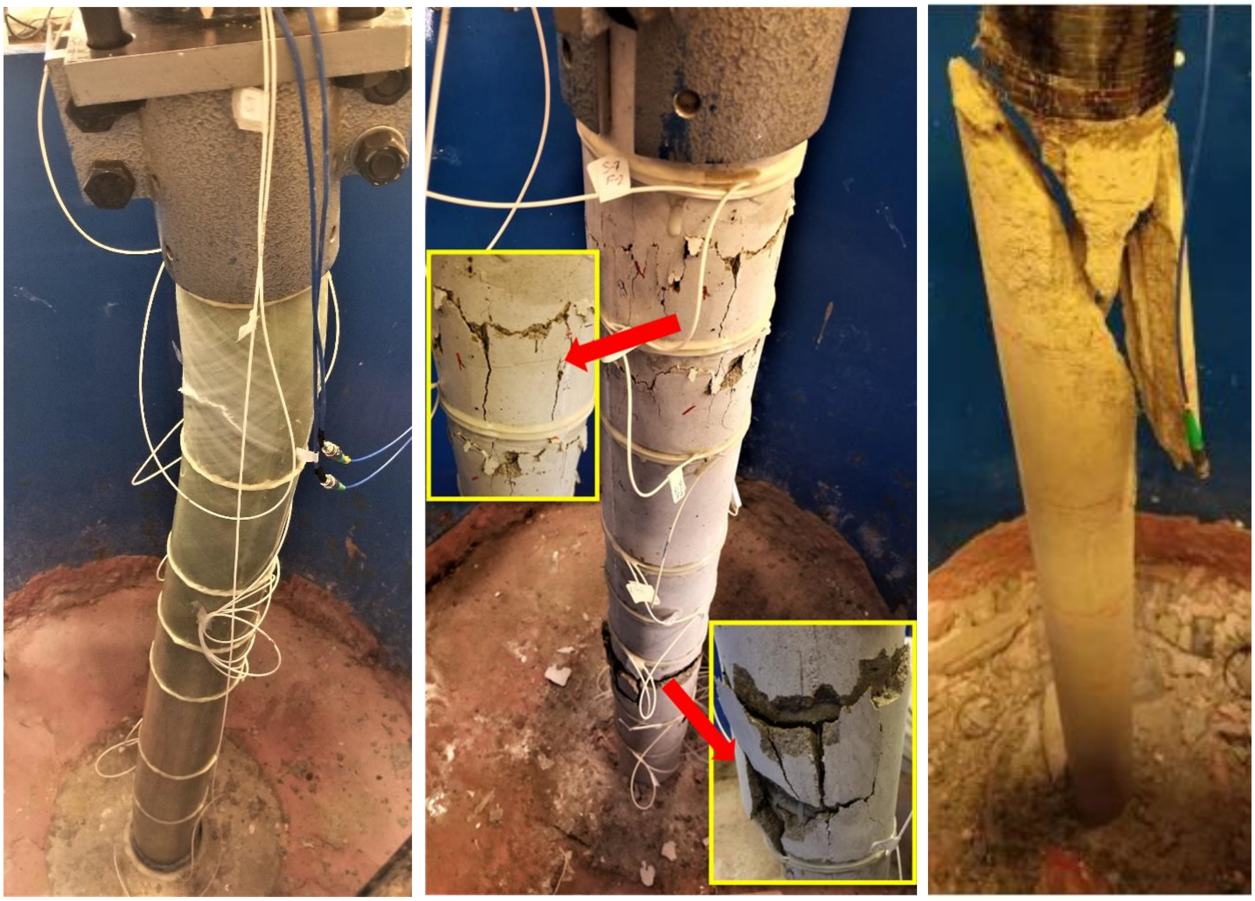

(a) (b) (c)

Fig. 12. Failure modes of FRP-SSC model piles under static loading: (a) Pile 2, (b) Pile 3, and (c) Pile 4

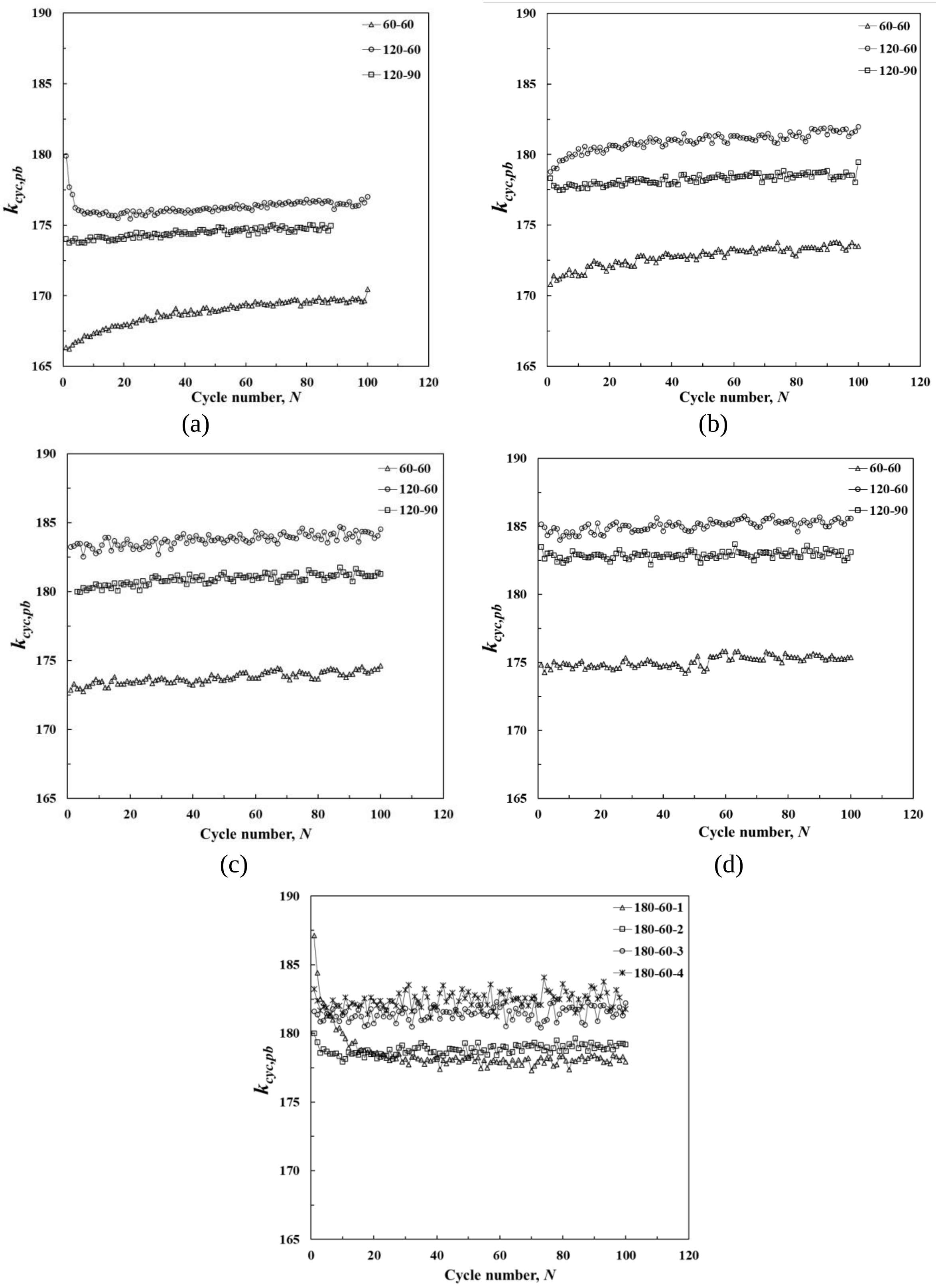

(a) (b) (c) (d) (e)

Fig. 13. Variation of pile body stiffness of pile 2 under different cyclic loading series: (a) Series 1, (b) Series 2, (c) Series 3, (d) Series 4, and (e) Series 5

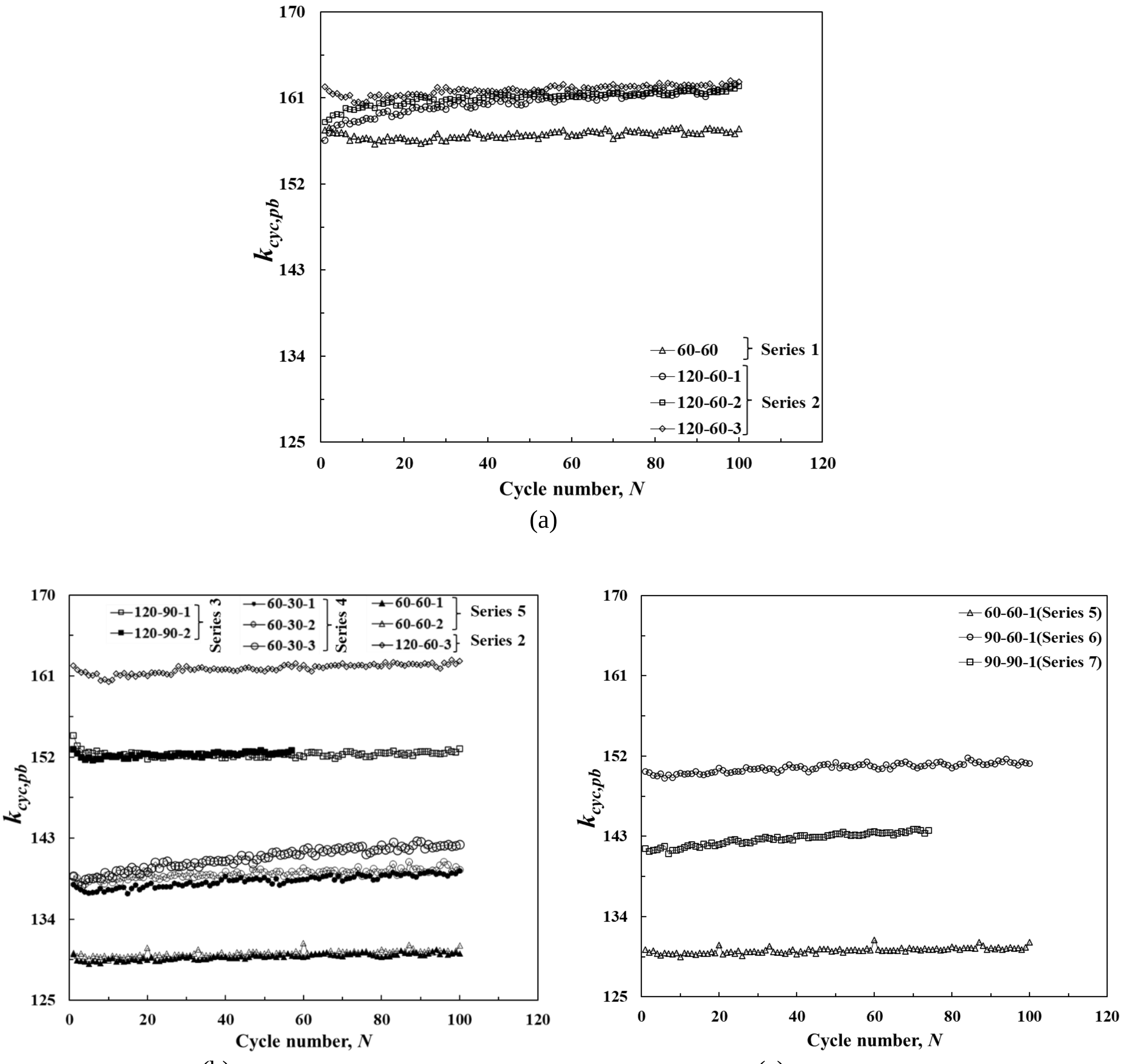

(a)

(b)

(c)

Fig. 14. Variation of cyclic stiffness of Pile 3 under different cyclic loadings: (a) Series 1 and 2, (b) Series 3, 4, and 5, and (c) Series 6 and 7

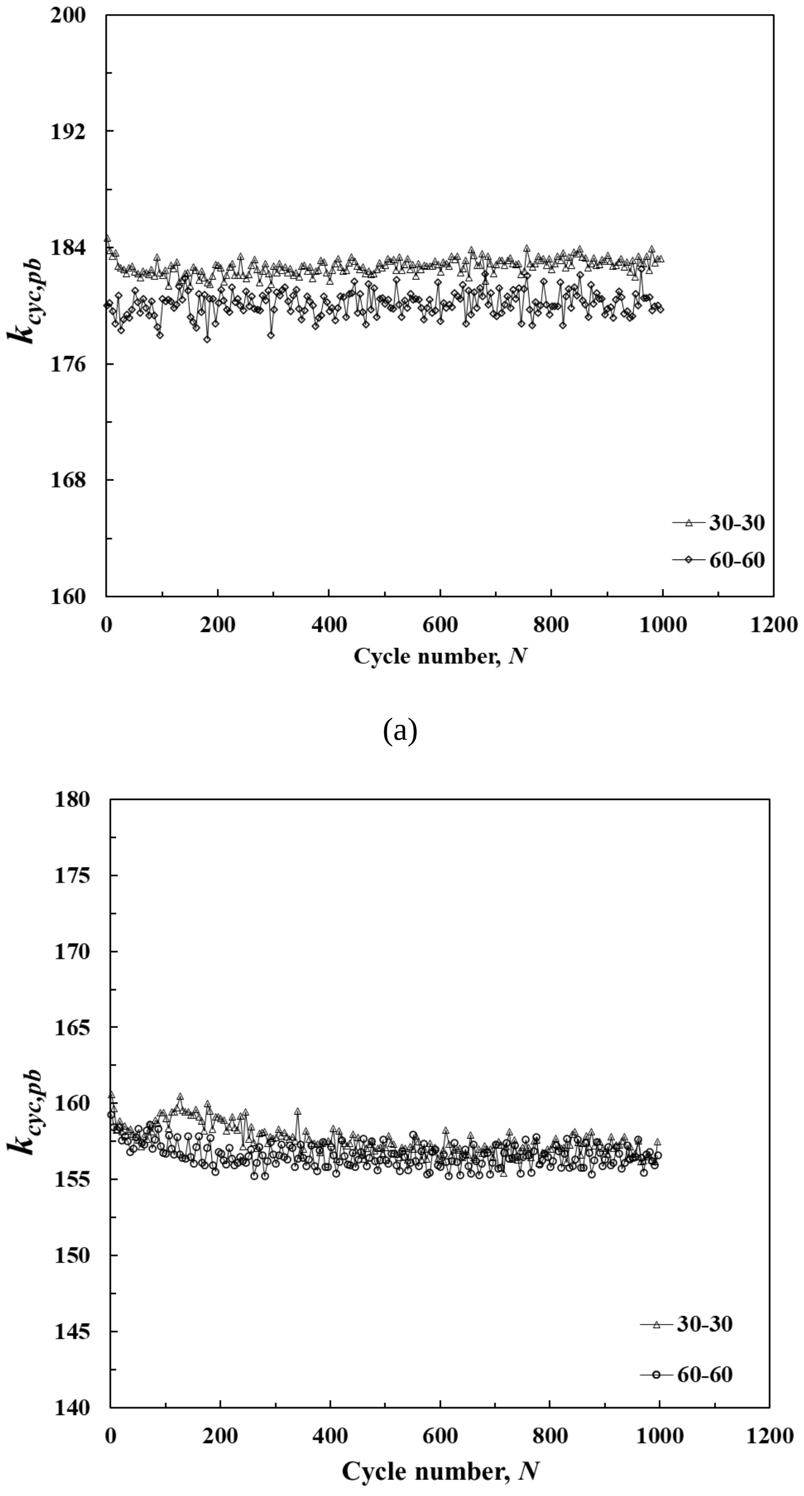

(a)

(b)

Fig. 15. Variation of cyclic stiffness of (a) Pile 4 and (b) Pile 5 under cyclic loading

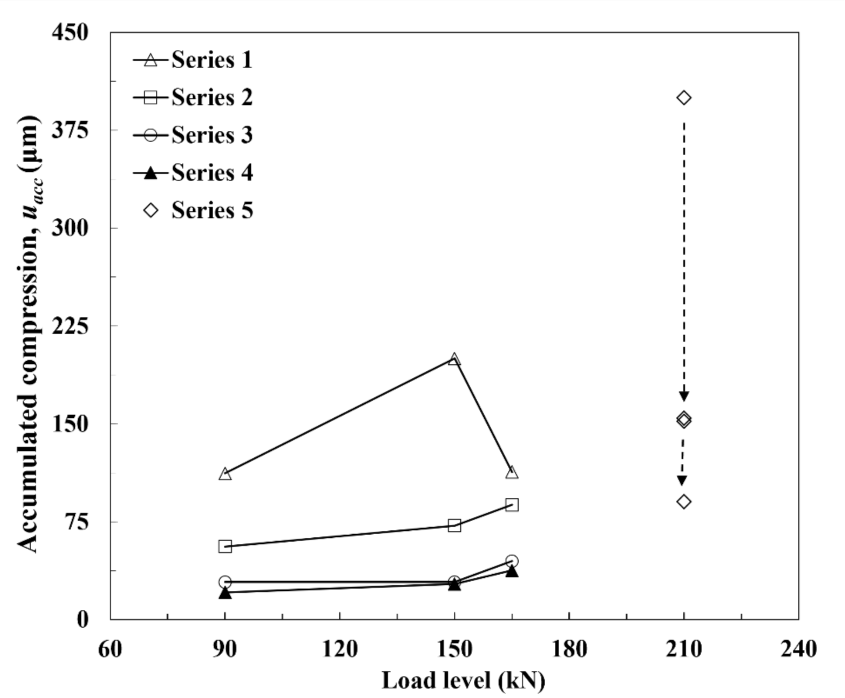

Fig. 16. Compression accumulation within pile body under different cyclic loading conditions

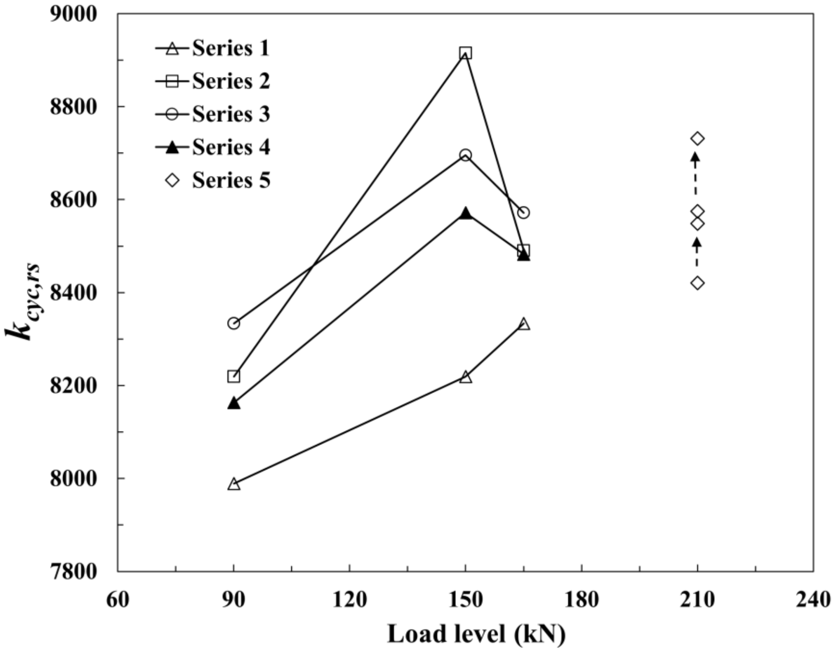

Fig. 17. Stiffness variation of the socket under different series of cyclic loadings

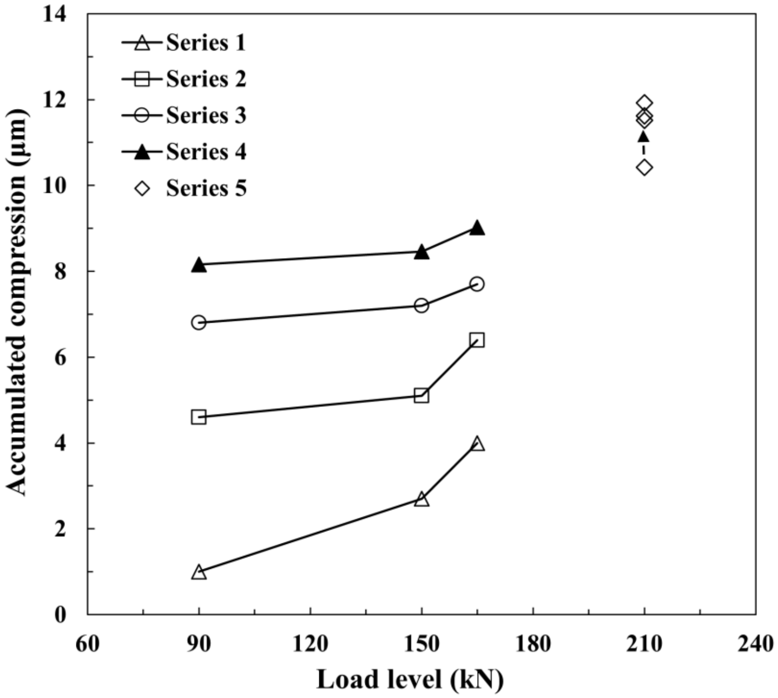

Fig. 18. Accumulated compression of Pile 2 within the rock socket under cycling loadings

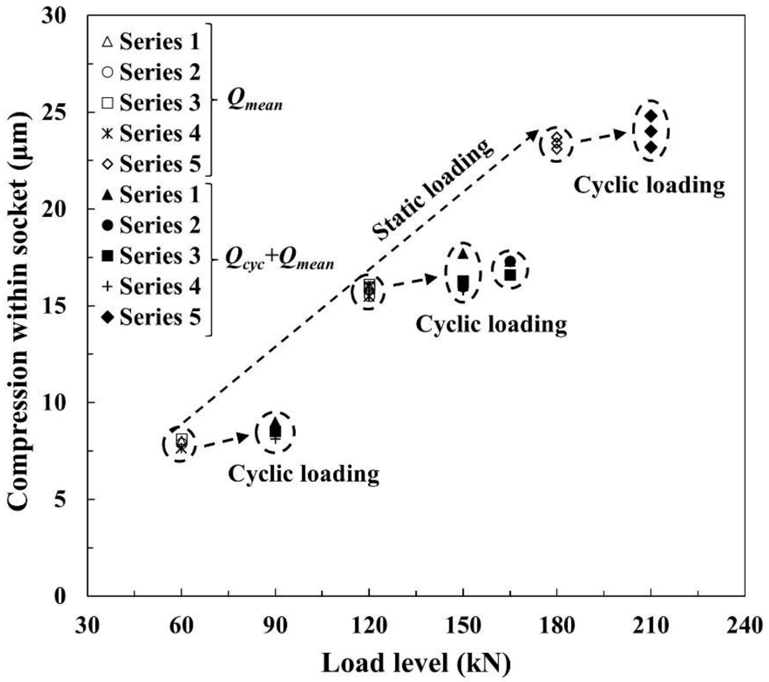

Fig. 19. Compression of model pile within the socket recorded at static loading and cyclic maximum loading conditions

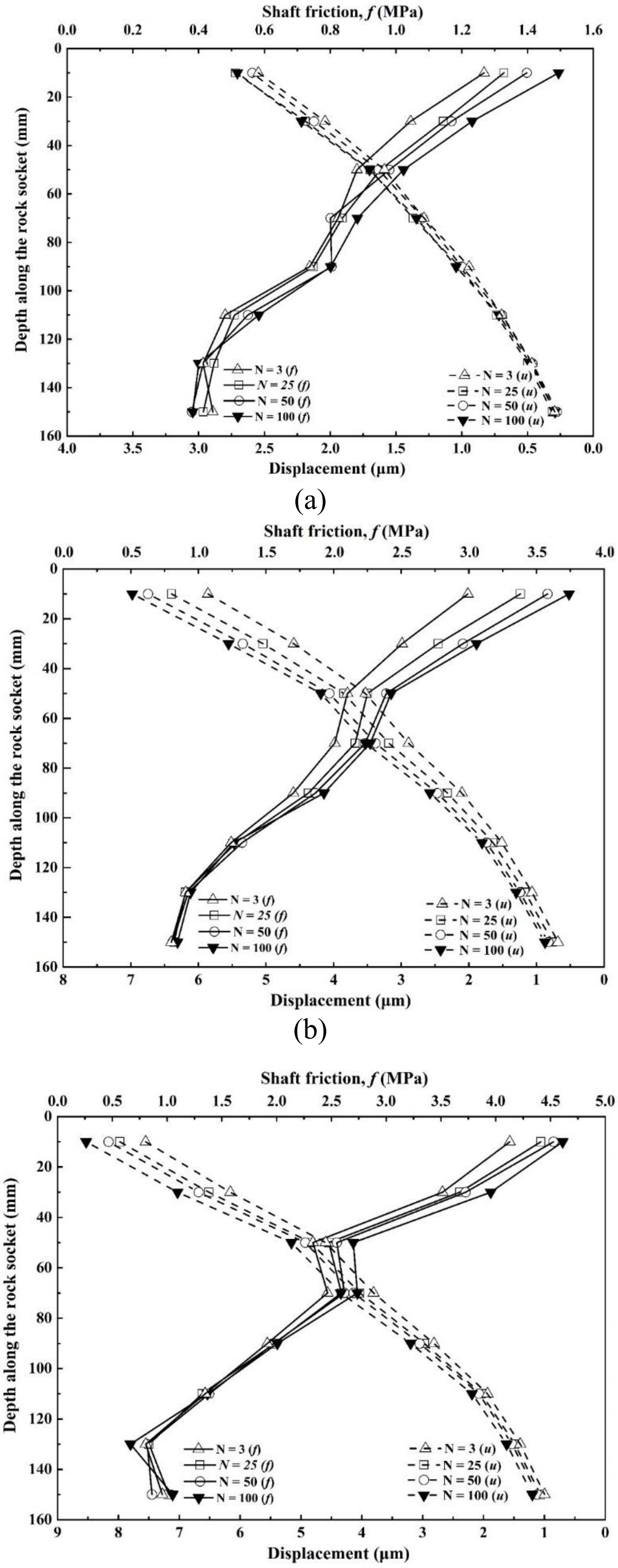

Fig. 20. Mobilization of shaft friction and displacement along depth for different loading cycles on Pile 3: (a) 60-60, (b) 120-60, and (c) 120-90

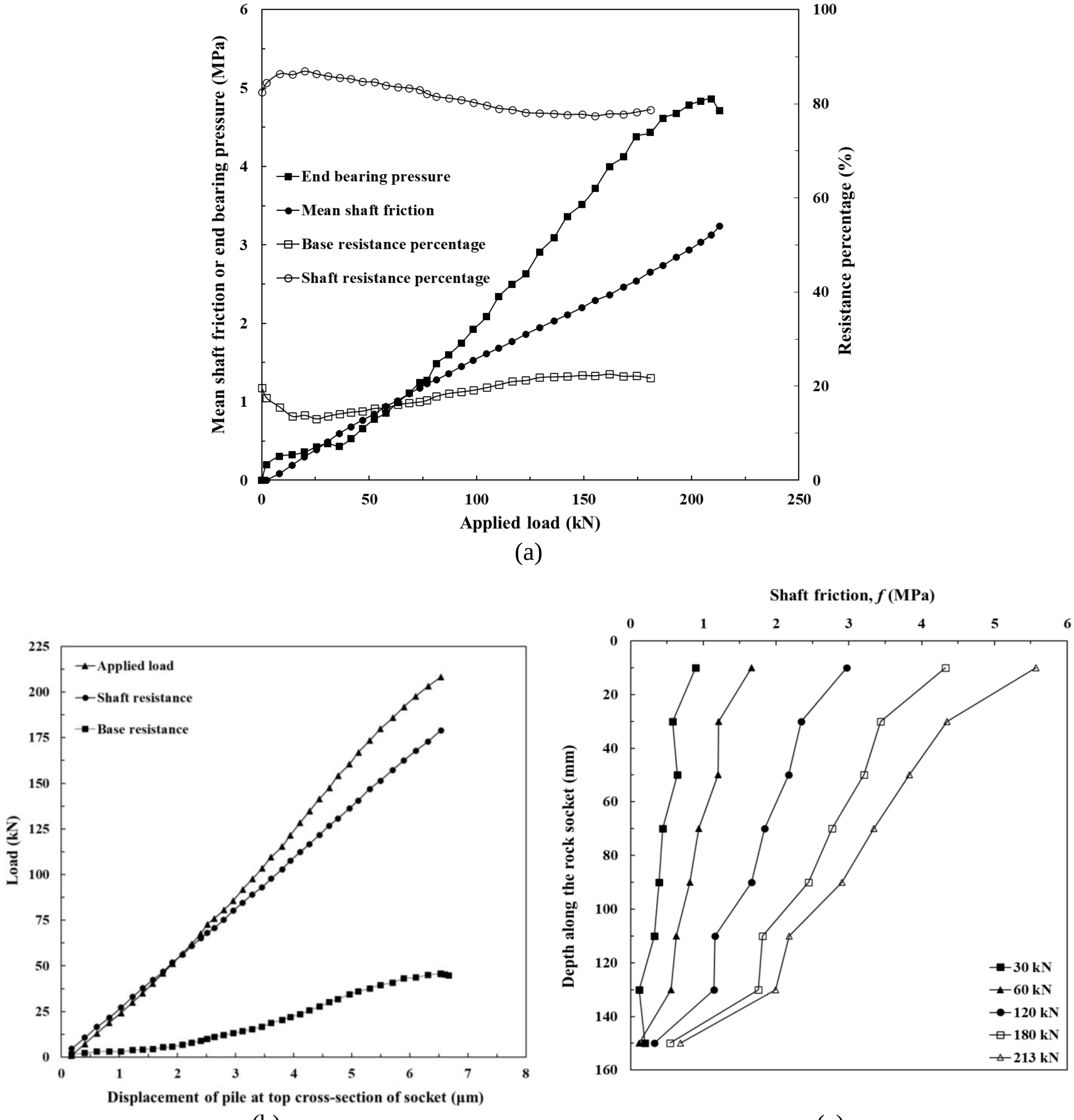

(a)

(b)

(c)

Fig. 21. Socket response of Pile 3 under static loading: (a) mean shaft friction, end bearing and resistance percentage against static load, (b) shaft resistance and base resistance against displacement, and (c) shaft friction at different loads along the socket depth